Reshaping the Role of CO_2 in Propane Dehydrogenation: From Waste Gas to Platform Chemical

Marco G. Rigamonti, Meera Shah, Thobani G. Gambu, Mark Saeys, and Michiel Dusselier*

ABSTRACT: The valorization of CO_2 appeals to the chemical industry due to the reduction in greenhouse gas emissions and the ability to offer more renewable products. Propylene production is the second largest process in the chemical industry, and it strongly depends on fossil fuel feedstocks. Coupling CO_2 reduction with propane dehydrogenation boosts conversion and produces CO, a valuable platform chemical currently synthesized by fossil-methane reforming. In this work, (i) we demonstrate the environmental benefits of coupling CO_2 with a life-cycle assessment under industrial conditions, potentially reducing emissions by 3 t_{CO2-eq} per ton of propylene produced. (ii) We screen supported catalytic materials—both known and novel—with a focus on propane and CO_2 reaction mechanisms under industrial reaction conditions of

400−700 °C and pressures of 1−6 barg (redox: V, Galinstan, In, Mo, Mn, Bi, Sb, Ta; nonredox: Cr, Ga, co, Al, Zn, Au, Zr, Ag, W, La, Cu; and some alloy combinations). We evaluate each material under the kinetic regime, and we quantify reaction, side reaction, and deactivation kinetics (coking, cracking, and dry-reforming), as well as the regeneration ability. We then classify them based on their dominant mechanisms (direct CO_2 assistance or indirect with H_2 via reverse water gas shift) and identify each catalyst's strengths and weaknesses. Finally, (iii) we correlate our database of experimental results of 22 active metals/metal oxides with the Tamman temperature and density functional theory (DFT)-based oxygen vacancy formation energies. We discovered that oxygen mobility plays a crucial role in the kinetics of reoxidation with CO_2 and the overall balance of active sites related to dehydrogenation and reoxidation.

KEYWORDS: CO_2-ODHP, LCA, Tamman, redox mechanism, propane dehydrogenation, CO_2 soft oxidation

INTRODUCTION

Propylene is the second largest bulk chemical produced globally, primarily feeding the ever-growing polymer industry. The production of propylene has steadily increased by 6% annually in the past 10 years,[1,2] and despite the 2019 coronavirus pandemic, it reached 130 t y^{-1} in 2020 and is expected to keep growing at a similar rate for the next decade.[3] Regarding propylene production, fluid catalytic cracking (FCC) and steam cracking (SC) dominate the industrial panorama, converting naphtha into a mixture of olefins—primarily ethylene and propylene—while the coal-to-olefin (CTO) process relies on coal to synthesize syngas, methanol, and ultimately olefins.[4] Various life-cycle analyses (LCAs) estimate the associated environmental impact (EI) costs for each technology. (i) FCC generates the least amount of greenhouse gas (GHG) emissions with 1.5−1.6 kg_{CO2-eq} kg_{C3H6}^{-1} and fossil fuel depletion (FD) with 1.4−1.5 kg_{oil-eq} kg_{C3H6}^{-1} but only accounts for 25−35% of the global production of propylene. (ii) SC represents 40−50% of propylene production with comparatively modest emissions of 2.1 kg_{CO2-eq} kg_{C3H6}^{-1} and 1.6 kg_{oil-eq} kg_{C3H6}^{-1}. (iii) CTO,

instead, is the most polluting of all three processes relative to the amount of propylene produced (10%): GHG = 9−12 kg_{CO2-eq} kg_{C3H6}^{-1} and FD = 2.9−3.7 kg_{oil-eq} kg_{C3H6}^{-1}.[5−8] Dehydrogenation of (fossil) propane (DHP) offers an alternative as a selective on-purpose production of propylene with similar EI to FCC, with EI variabilities based on local heat supplies (shale gas vs coal vs electricity): GHG = 1.7 kg_{CO2-eq} kg_{C3H6}^{-1} (North America),[1] 2.0 kg_{CO2-eq} kg_{C3H6}^{-1} (China),[9] 2.2 kg_{CO2-eq} kg_{C3H6}^{-1} (electric),[10] and FD = 1.2−1.6 kg_{oil-eq} kg_{C3H6}^{-1}. The technology was introduced in the 1990s to bridge the growing gap in the demand for this chemical. Several commercial catalytic processes exist today, satisfying 15−20% of the global propylene production: Catofin,

Table 1. Commercial DHP technologies[a]

process (licenser)	catalyst, *wt %*	reactor configuration	heat supply	T, °C	P, bar	X_{C3H8}, %	SV, h^{-1}
Catofin (CB&I Lummus-Clariant)	18−20% Cr_2O_3/Al_2O_3 with a 1−2% K promoter	8 parallel adiabatic fixed beds	coke burn-off	550−650	0.3−0.5	45−50	0.2−1
FBD (Snamprogetti-Yarsintez)	core−shell: 12−20% Cr_2O_3/Al_2O_3 with 1−2% K and 1−2% SiO_2 for attrition resistance	fluidized bed similar to FCC designs	coke burn-off	550−600	1.1−1.5	40	0.2−1
PDH (Linde-BASF)	18% Cr_2O_3 on Al_2O_3 with 0.25% Zr, K; or Pt-Sn on hydrotalcite Mg(Al)O; Pt-Sn/ZrO_2	3 parallel isothermal fixed beds	furnace	590	1.0	30	1−4
Oleflex (Honeywell UOP)	0.3% Pt/Al_2O_3 with Sn promoter	4 adiabatic moving beds in series	furnace	550−650	1.1−3.0	35−40	1−2
Star (Thyssenkrupp-Uhde)	0.2−0.6% Pt/CaO-$ZnO\cdot Al_2O_3$	multiple fixed beds and adiabatic oxy-dehydrogenation	furnace	550−680	5.0−6.0	40	2−3

[a]Star adds O_2 to drive forward the equilibrium. T and P: reaction temperature and pressure. X_{C3H8}: propane single pass conversion. SV: weight hourly space velocity, kg_{C3H8} h^{-1} $kg_{catalyst}^{-1}$.[11−14]

fluidized-bed dehydrogenation (FBD), propane dehydrogenation (PDH), Oleflex, and Star (Table 1).

The DHP reaction is endothermic and thermodynamically limited below 500 °C. However, working above this temperature causes coke to form, resulting in catalyst fouling, representing the main reversible deactivation mechanism and byproduct of the reaction. Fresh and recycled propane feeds multiple reactors that switch between reaction and regeneration, in order to maintain continuous productivity. At present, only two active materials dominate the industrial market—chromium and platinum—each with similar activity and selectivity (85−90%), but with design differences based on heat supply and in situ catalyst regeneration methods. Catofin and FBD, based on Cr oxide catalysts, opt for frequent catalyst regeneration (time scale: hours), and coke combustion in air/O_2 provides the heat requirement for the reaction. PDH, Oleflex, and Star rely instead on Pt catalysts, which accumulate less coke, thus requiring an external heating source and a longer time-on-stream (TOS) between cycles (time scale: days). Each regeneration cycle shortens the catalyst lifespan by irreversibly deactivating Cr and Pt, which generally last 1−2 and 3 years, respectively. In the case of Cr, hotspots induce metal diffusion into the support lattice, creating solid solutions of inactive α-Cr_2O_3-Al_2O_3[15] as well as the formation of low-surface-area crystalline α-Cr_2O_3—difficult to reoxidize and redisperse.[16] Pt instead sinters[17] and requires expensive oxychlorination conditions to mitigate this process during regeneration.[18]

With regard to the nature of the active phase, bulk α-Cr_2O_3 is thermodynamically the most stable oxide at the reaction temperature but is inactive and needs dispersion on a support, such as γ-Al_2O_3, which can stretch the active metal oxides in high-valent polychromate species Cr^{6+}, Cr^{5+}, and Cr^{3+}.[19,20] Grafted polychromates are highly active but more selective to cracking and reforming, and also unstable, quickly reducing to Cr^{3+} in a matter of minutes. Cr^{3+} is the active site for DHP, which proceeds via a Langmuir−Hinshelwood mechanism of C−H cleavage and H-abstraction.[21,22] Within hours, the active sites reduce to less active Cr^{2+} species, requiring catalyst regeneration.[23] Other supports such as mesoporous silica (SBA-1, SiO_2 gels) have a higher specific surface area and are more inert than alumina, allowing better dispersion of chromium oxides and a higher propylene selectivity.[24,25] However, the low thermal conductivity of mesoporous SiO_2 (0.1 vs 10 W m^{-1} K^{-1} of γ-Al_2O_3) requires more expensive

reactor designs for heat management. Furthermore, a faster sintering deactivation is observed during numerous regeneration cycles;[26] hence, no industrial application has been found using SiO_2 as a support.

Concerning Pt-based catalysts, Al_2O_3 is the support of choice. The type of alumina used depends on their acidic and morphological properties: α- and θ-alumina supports possess relatively less Brønsted and Lewis acid sites than γ-alumina and are more stable against sintering and coking but also have lower surface areas. Strong Brønsted acid sites are also responsible for coking via direct alkane protonation and propylene condensation. The support forms "hard" aromatic coke (graphitic), while "soft" aliphatic coke (amorphous-polymeric) adsorbs on Pt metal sites. The presence of H_2 in the reaction gases weakens the support's Brønsted acid sites, converting them to Lewis sites, thus reducing coke formation.[27] Strong Lewis acid sites, on the other hand, induce alkane cracking via hydride abstraction and the generation of carbenium ion-activated complexes. Therefore, alkali metal promoters (K, Sn, Mg, Zn) are added to saturate the acid sites of the support and mitigate sintering.[28] The surface chemistry of highly dispersed Pt proceeds via an irreversible dissociative adsorption of the alkane on two Pt atom active sites (rate-determining step), followed by the second H-elimination (in quasi-equilibrium).[29]

At present, the CO_2-assisted oxidative dehydrogenation of propane (ODHP) has no industrial application. However, it has great potential, as the presence of CO_2 drives the reaction equilibrium forward and converts this greenhouse gas into CO—an important platform chemical.[30−32] O_2 is a 100-fold stronger oxidizing agent than CO_2 and can render the process autothermal;[33] however, less selective (60% for V/SiO_2) and catalytic materials struggle to avoid total combustion catalytic pathways at high conversions.[34] The hexagonal boron-nitride catalyst has shown a remarkable improvement in selectivity (80% at 8% conversion) thanks to a different mechanism versus the classical surface C−H bond activation, where radical reactions activate propane in the gas phase; however, also in this case, selectivity drops as the conversion increases (60% at 35% conversion).[35] CO_2 has the chemical potential for partially reoxidizing the reduced metal oxides formed during ODHP, replenishing oxygen vacancies.[4] For redox materials like V oxides, this occurs via a Mars−van Krevelen (MvK) mechanism,[36−38] in which the C−H bond activation proceeds via a lattice oxygen abstracting a H atom from an adsorbed
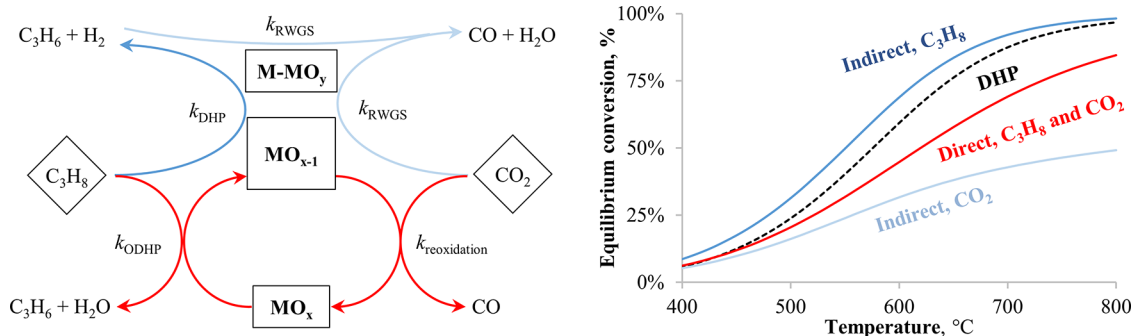
Figure 1. Left: Forward reaction mechanism: highly valent metal oxides (MO_x) directly convert propane and CO_2 via a redox mechanism (red). The reduced active site (MO_{x-1}) requires CO_2 reoxidation to close the catalytic cycle. Reduced species and nonredox metal or metal oxides (M-MO_y) participate in the separate conversion of propane and CO_2 via DHP (blue) and rWGS (light blue), respectively. For chromium oxides, the kinetics benefit from the presence of CO_2 ($k_{ODHP} > k_{DHP}$), which is efficiently converted to CO ($k_{RWGS} > k_{ODHP}$). However, Cr^{6+} is short-lived and regeneration does not occur due to thermodynamic (chemical potential of CO_2 oxidation) or kinetic constraints ($k_{ODHP} \gg k_{reoxidation}$), leading to fast deactivation.[42,48,49] Right: Equilibrium conversion for 0.5 bar of propane with 0.5 bar of CO_2 (Aspen Hysis); the nonoxidative DHP is also shown (0.5 bar of pure propane). The indirect mechanism assumes the presence of DHP and rWGS equilibria, and the direct mechanism assumes only ODHP equilibrium.

Table 2. Chemical Reactions Considered in This Study and Corresponding Gibbs Free Energy of Reaction at Standard Condition (1 bar, Stoichiometric Composition) Calculated with Aspen Hysis[a]

Chemical equation		Gibbs free energy of reaction plot
$C_3H_8 + CO_2 \leftrightarrow C_3H_6 + CO + H_2O$	(1)	
$C_3H_8 \leftrightarrow C_3H_6 + H_2$	(2)	
$CO_2 + H_2 \leftrightarrow CO + H_2O$	(3)	
$CO_2 + C \leftrightarrow 2CO$	(4)	
$C_3H_8 \leftrightarrow CH_4 + C_2H_4$	(5)	
$C_3H_8 + 3CO_2 \leftrightarrow 6CO + 4H_2$	(6)	
$C_3H_6 \leftrightarrow 3C + 3H_2$	(7)	

[a]We considered propylene decomposition as the main reaction pathway forming coke as the allylic C−H bond is weaker than that of propane (370 kJ mol^{-1} vs >400 kJ mol^{-1}).[50]

propane molecule coordinated with a neighbor lattice oxygen.[39] For highly valent Cr oxide, there is no consensus: either via a Langmuir−Hinshelwood mechanism[40] or via MvK.[41] For nonredox catalysts (Pt or Ga_2O_3) and reduced metal oxides (like, for example, Cr^{3+}), it is believed that CO_2 is unable to reoxidize them to higher-valent species (such as Cr^{6+}) and propane catalysis proceeds via C−H cleavage and H-abstraction.[42] There, CO_2 consumes surface hydride species and H_2 via the reverse water gas shift (rWGS) reaction,[43,44] while the reverse Boudouard reaction reforms soft coke into CO,[45,46] with CO_2 promoting propylene desorption, thus lowering coke formation.[47]

Under a carbon capture and utilization strategy, revamping preexisting DHP infrastructures to integrate the ODHP process and reduce the environmental footprint of propylene can be achieved without major CAPEX investments required for a grassroots installation. In this scenario, redox catalysts appear more interesting, as they would promote a "direct" CO_2 reaction mechanism consuming propane and CO_2 in equal amounts (Figure 1 red—Table 2 reaction 1: ODHP). Instead, in the "indirect" mechanism, DHP and rWGS coexist in series (Figure 1 blue and cyan—Table 2 reaction 2: DHP and 3: rWGS), maximizing propylene yield but at a lower CO_2 conversion.

The presence of CO_2 however consumes surface H_2 (a benign specie that reduces coke formation under pure-DHP conditions) via rWGS, and CO_2 also enables the dry-reforming of propane (DRP) side reaction. This complex thermodynamic system requires a selective catalyst that can operate at high T (500−700 °C) and ideally under steady-state conditions, avoiding intermittent catalyst regeneration (Table 2). A number of studies have already investigated DHP catalysts operating in the presence of CO_2, but often without monitoring the conversion of CO_2 itself, due to past scientific interest in hydrocarbon selectivities rather than permanent gas quantification, which requires a gas chromatography system with a FID channel for the first and a TCD for the second. Given the prevalence of this greenhouse gas and the potential partial (C)CU nature of this reaction, we set out to investigate ODHP from a CO_2 utilization perspective.

■ MATERIALS AND METHODS

The Supporting Information (SI) contains sections for material, methods, and detailed analysis for each active metal tested as well as complementary figures and tables (numbered nS).
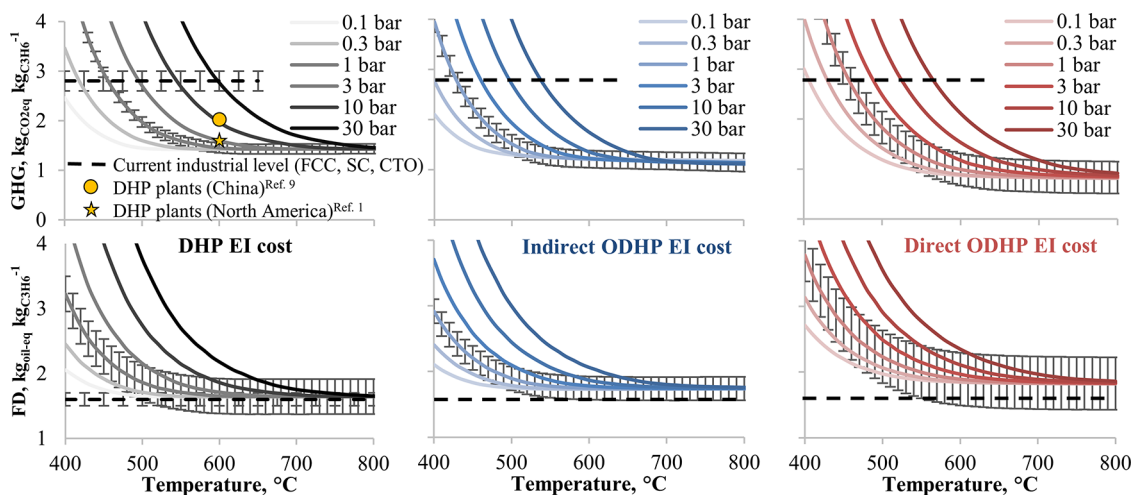
Figure 2. LCA with sensitivity analysis at various T and P is used to calculate the EI costs (GHG and FD) for the production of 1 kg of propylene from a DHP plant (black, left columns). I-ODHP with a catalyst that enables an indirect mechanism (blue, center). D-ODHP via a direct mechanism (red, right). Error bars at 1 δ associated with the EI database index's variability; other isobar curves have similar uncertainties. Current industrial levels are a weighted average of FCC, SC, and CTO—from the literature.

■ RESULTS AND DISCUSSION

We divide this section into three chapters: (i) an LCA to investigate the potential benefits of ODHP; (ii) a screening test of catalytic materials—both known and novel to ODHP—in realistic conditions focusing on their direct or indirect behavior; and (iii) the correlation between the Tamman temperature and oxygen mobility, playing an important role in the kinetics of reoxidation with CO_2 of the active sites.

Life-Cycle Analysis. We first wanted to calculate how the addition of CO_2 to a propane gas stream would influence GHG and FD compared to a modeled DHP plant and current industrial levels. We simulated (i) a DHP plant running on pure propane (DHP reaction, Figure 1S), (ii) an ODHP plant converting equimolar propane and CO_2 via an indirect mechanism (DHP + rWGS, Figure 2S), and (iii) a third one via a direct mechanism (ODHP, Figure 3S). Each system reached thermodynamic equilibrium, and we calculated the EI costs related to reagent gas feeding and utility consumption for splitting each product gas to at least 97% purity. Note that we have used the average CO_2 intensity per kWh for electricity from the Belgian grid (0.22 kg_{CO2-eq} kWh_{el}). We then proceed to evaluate different scenarios where we change the reaction T and P (Figure 2).

Low P and high T favor all three systems, in agreement with the thermodynamics of the reactions involved: (O)DHP reactions increase the number of moles (by a factor of 2 or 1.5) and are endothermic in nature (DHP has $\Delta H_{25°C}{}^r$ of the reaction = +124 kJ mol^{-1}, rWGS has $\Delta H^r{}_{25°C}$ = +41 kJ mol^{-1}, and ODHP has $\Delta H_{25°C}{}^r$ = +164 kJ mol^{-1}). Temperatures lower than 500 °C diminish productivity, which in turn increases the EI costs related to separation and purification of the unreacted feed. Temperatures higher than 700 °C lead in all cases to a theoretical minimum with complete conversion and minimal separation costs; however, in practice, they are not achievable, as undesirable side reactions, which have not been accounted for in this simulation—coking, cracking, and reforming—become predominant. On average, commercial PHD plants operate at around 600 °C with a 40% conversion per passage (Table 1). At this temperature, the EI curves plateau at a minimum (1.5 kg_{CO2-eq} $kg_{C3H6}{}^{-1}$) as long as the pressure is below 3 bar, indicating that operating at lower pressures lessens the environmental impact of all three processes. When we compare our LCA with the state of the art, we observe that China primarily uses coal to supply heat to the reaction and scores higher in GHG emissions (2.0 kg_{CO2-eq} $kg_{C3H6}{}^{-1}$). North American plants use methane and shale gas, which drives the GHG emissions lower (1.7 kg_{CO2-eq} $kg_{C3H6}{}^{-1}$) and which is in line with our LCA modeling, since we also use methane to provide the heat requirements of the reaction (methodology under the SI).

In general, operating gas-phase reactors at high pressure intensifies the process because it allows one to size down units and to lower investment costs while maintaining the same level of productivity.[51] Also, separation units may benefit from high-pressure regimes. In particular, both propane/propylene distillation and pressure swing adsorption (an industrial alternative to distillation) benefit from higher process pressures: the first one in terms of energy saving when operating at 13 bar (because of the higher boiling points of the liquids)[52] and the second one in terms of propylene recovery (from 84 to 89%) when the adsorption pressure increases from 2.5 bar to 4 bar.[53] However, in our modeling, we observe that to maintain the same level of EI, any increase in pressure leads to an increase in temperature—because of the thermodynamics of the equilibrium. In this context, a catalyst capable of operating above 600 °C would make the process more economically appealing as it would enable operating in this higher-pressure regime, lowering CAPEX and OPEX.

Taking T = 600 °C and P = 1 bar as reference reaction conditions, we see a significant GHG improvement when operating under ODHP conditions (Figure 2 top row and Table 3).

CO_2 capture and utilization are the main factors driving the EI benefit compared to DHP as it reduces GHG by 40% on D-ODHP. A breakdown of the GHG contributions indicates that propane is the main GHG contributor (50%), followed by thermal heat (30%) and electricity (20%) (Figure 3).

On the other hand, DHP and ODHP do not offer any improvements when analyzing FD (Figure 2 bottom row and Table 3). The main FD contributor in this case is propane

Table 3. (Top) EI Cost of Current Industrial Practices (Weighted Average of FCC, SC, CTO—from the Literature) and Calculated from Our Three Case Scenarios, DHP, Indirect ODHP, and Direct ODHP, at T = 600 °C and P = 1 bar, to Produce 1 kg of Propylene (Functional Unit)[a]

EI cost	current	DHP	I-ODHP	D-ODHP
GHG, kg_{CO2-eq} kg_{C3H6}^{-1}	2.8(2)	1.5(1)	1.2(2)	1.0(3)
FD, kg_{oil-eq} kg_{C3H6}^{-1}	1.6(1)	1.7(2)	1.7(2)	1.9(2)
Net EI cost	current	DHP	I-ODHP	D-ODHP
GHG, kg_{CO2-eq} kg_{C3H6}^{-1}		−1.9(3)	−2.6(3)	−3.4(4)
FD, kg_{oil-eq} kg_{C3H6}^{-1}		−0.1(2)	−0.4(2)	−0.8(2)

[a](BOTTOM) Net EI costs discounting also H_2, CO, and propylene. In parenthesis, 1 δ variability.
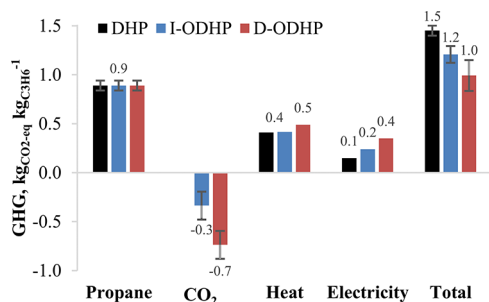

Figure 3. GHG cost breakdown and 1 δ variability. CO_2 capture from industrial flue gas (this study) is the best-case scenario to reduce emissions: GHG = −0.70(15) kg_{CO2-eq} kg_{CO2}^{-1}, but it is highly variable. CO_2 capture from air instead (not used here) is less profitable but also less dependent on external factors and, therefore, less variable: GHG = −0.50(5) kg_{CO2-eq} kg_{CO2}^{-1}.

(75%), followed by thermal heat (10%), electricity (10%), and ultimately CO_2 (5%, Figure 4S).

From the perspective of a levelized energy consumption per kg of propylene produced, we calculate that thermal heat supplied to the reactor and column reboilers (modeled as natural gas combustion) increases heat requirements from 6.3 MJ kg_{C3H6}^{-1} (DHP and I-ODHP) to 7.3 MJ kg_{C3H6}^{-1} (D-ODHP). Instead, a heavier increase occurs for electricity consumption to drive the cryogenic separation of H_2, CO, and CO_2 at the condensers: 2.9 $MJ_{el.}$ kg_{C3H6}^{-1} (DHP), 4.4 $MJ_{el.}$ kg_{C3H6}^{-1} (I-ODHP), and 6.9 $MJ_{el.}$ kg_{C3H6}^{-1} (D-ODHP, Table 2S). From an environmental point of view, despite the more energy-intense process, the EI benefits from the consumption of CO_2 still offset the EI costs associated with the separation (Figure 3). However, from an economical perspective, this highlights the key importance of finding inexpensive and low-EI electric sources to enable CO_2 utilization in future industrial applications. Considering the costs of Belgian utilities, shifting from a DHP to a D-ODHP process would increase these OPEX by 0.15 Euro kg_{C3H6}^{-1}, but it would also allow the industry to utilize coproduced CO (0.67 kg kg_{C3H6}^{-1}) as a platform chemical for additional purposes.

When we consider the net EI (Figure 5S), we see a greater difference between technologies. At 600 °C, 1 bar, DHP produces propylene and H_2 at lower GHG emissions compared to state-of-the-art industrial methods for synthesizing the same products (SMR steam methane reforming for H_2 and FCC, SC, and CTO for propylene), saving 1.9(3) kg_{CO2-eq} kg_{C3H6}^{-1} (Table 3). I-ODHP further improves the score because it also converts CO_2 to CO, and D-ODHP achieves the greatest EI savings of 3.4(4) kg_{CO2-eq} kg_{C3H6}^{-1} because of the higher yield in CO, compared to the indirect mechanism (45 vs 32%). In this scenario, the ideal catalyst would promote
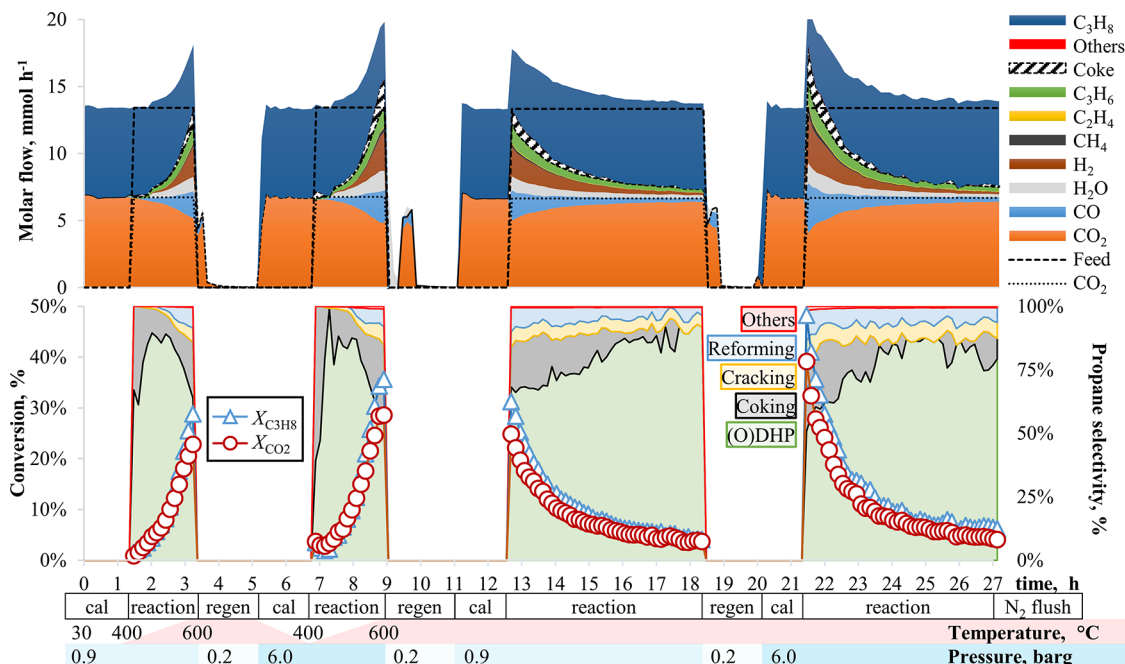

Figure 4. VO_x/Al_2O_3 tested under screening conditions during 27 h (graph to scale). Top: Molar flow evolution of species measured via GC and calculated from carbon and oxygen balances (coke and H_2O). Bottom: Conversion (symbols) and reaction selectivity from propane (colored area); the noise in the data is due to instrumental precision, with the highest at low X. We calibrate "cal" the inlet gas mixture via a bypass (100 N mL min^{-1}: 2.5% propane, 2.5% CO_2, 95% inert), followed by reaction and regeneration "regen" (air: 10 N mL min^{-1}). GHSV = 40000 N mL mL_{cat}^{-1} h^{-1}; WHSV = 1.5 $g_{propane}$ g_{cat}^{-1} h^{-1}. Separate rWGS reactions are reported in the SI, replacing propane with H_2 (Figure 12S).

a direct mechanism (ODHP) while suppressing WGS. In fact, in the absence of the WGS reaction, no CO is consumed to generate H_2 and CO is a chemical with a higher EI compared to H_2 (3-fold GHG and 5-fold FD). In terms of net FD instead, DHP technology does not improve the situation with savings of 0.1(2) kg_{oil-eq} kg_{C3H6}^{-1}. Nevertheless, I- and D-ODHP achieve greater scores with savings of 0.4(2) and 0.8(2), respectively.

This limited LCA thus shows great promise for CO_2-ODHP, especially via a direct mechanism, as an on-purpose route for reducing the environmental impact of propylene manufacturing. The potential for negative net emissions is quite large, provided that the coproduced CO replaces (in part) the established but quite polluting route of SMR.[6] Moreover, EI costs can be driven down even further by coupling H_2 with CO (syngas), avoiding their separation, and the use of better unit operations: pressure swing adsorption[54] and membrane for the separation of gases.[55,56] It should be noted that the LCA scenarios assume thermodynamic yields and ideal selectivities, although imposing a fixed 80% approach to equilibrium, which simulates typical industrial single-pass conversions, did not significantly alter the results (Table 2S). To come close to those performances, catalytic design is key. Since the direct mechanism represents the best environmental scenario, we therefore screened catalytic materials in search of redox MvK pathways.

Catalyst Screening. Given that γ-alumina is the support material of choice in industrial catalysts, herein 22 different active metals and mixed-metal oxides were impregnated on a commercial γ-Al_2O_3 (SASOL, SCCa-5/200) at a loading of 1.3 mmol of metal (M) per gram of catalyst support (with the exception of Au, Cu, and Ru; see the SI), and 200 mg of the calcined materials was tested. Assuming the formation of a monolayer of the thermodynamically most favorable metal or metal oxide during air calcination, this loading roughly corresponds to 50−80% surface area coverage of γ-Al_2O_3 (Table 6S) and should avoid its overloading.[4,30,57,58] Weak catalysts have activity that equate to that of the bare support, and we chose a reference reaction condition of 600 °C and 0.9 barg to compare the data because of the industrial significance. Moreover, Al_2O_3 shows minimal activity under these conditions: conversion $X_{propane}$ = 2%, X_{CO2} = 1%, and space time yield $STY_{propylene}$ = 0.4 mol h^{-1} kg_{cat}^{-1} (Table 3S and Figure 10S). To demonstrate our catalytic protocol—which includes temperature ramps (T ramp) to study the kinetic and isothermal time-on-stream (TOS) tests for the deactivation in a plug-flow fixed-bed reactor both under two levels of pressure P—we detail the performance of VO_x on alumina in the next section (Figure 4). Four distinct materials come forward, which we discuss in more detail (Figure 7). Afterward, a wide screening in terms of supported metals and metal oxides is demonstrated (Figure 9), and correlations with their intrinsic properties are explored (Figure 11).

VO_x/Al_2O_3. Kinetic isotopic experiments have proven that the redox MvK O_2-ODHP mechanism occurs with vanadium oxide catalysts.[59] We tested a VO_x/Al_2O_3 catalyst up to 600 °C during CO_2-ODHP, and between 400 and 500 °C, the reaction is the most selective for propylene and the catalyst converts propane and CO_2 in equimolar amounts, following the stoichiometry of a direct ODHP mechanism. We calculate the overall reaction selectivity (S_i) in relation to the propane feed, including all possible byproducts and side reactions, by grouping them in terms of the reaction mechanism. For

"(O)DHP" (green), we group the reaction that produces propylene, either via DHP or via ODHP. "Coking" (gray) monitors the accumulation of C calculated from carbon balance (CB) derived from the coking reaction. "Cracking" (yellow) measures CH_4 and C_2H_4, the products generated from the cracking of propane. "Reforming" (cyan) considers the CO generated from propane's carbon atoms during the DRP dry-reforming of the propane reaction. "Others" (red) groups the remaining species—mainly C_2H_6 from hydrogenation of C_2H_4, cyclopropane, and saturated/unsaturated C_4 (Figure 4). For our material, (O)DHP accounts for up to 90% of the recorded selectivity in the T-ramp experiments at low P and high P, with an optimum at 500 °C (green area in Figure 4). Whereas lower temperatures might induce transient adsorption of propane, which coupled with the instrumental sensitivity to measure small variations at low conversion, it leads to noise in the data and incomplete CB shown as coke formation. The hydrocarbon selectivity toward propylene ($S_{propylene}^{HC}$ excluding CO and coke formation) is greater than 98%.

Provided the reaction follows a direct ODHP pathway, ideally, no H_2 would be synthesized. However, it was found that for the VO_x/Al_2O_3 catalyst, 0.3 moles of H_2 are produced for each mole of propylene at 500 °C (H_2/propylene ratio, Figure 5 left, blue circles). This is due to (i) the hydrogen-
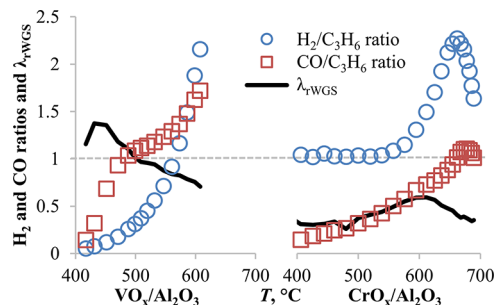

Figure 5. Direct mechanism catalyst (VO_x—left) produces 1 equiv of CO and no H_2, but side reactions and WGS equilibrium produce H_2; however, for the indirect one (CrO_x—right), this is the opposite. RWGS alone cannot explain the product distribution on the left as $\lambda_{rWGS} > 1$ and it follows a declining trend with T, rather than increasing (right). T-ramp data at 0.9 bar.

generating coking side reaction, which represents a selectivity of around 10% (see the gray area in Figure 4); (ii) DHP having a slower kinetic compared to ODHP but contributing in parallel to the generation of propylene and H_2 (Figure 1 left); and (iii) WGS, which equilibrates H_2 and CO balances in the stream.

Increasing the temperature from 500 to 600 °C increases exponentially the amount of hydrogen generated per mole of propylene to a 2.2 ratio. This is concomitant with an increased degree of coking as well as dry-reforming side reactions, being more active at high temperatures compared to ODHP (see activation energies for each reaction under the SI, Figure 8S). The CO/propylene ratio (Figure 5, red square symbols) also measures the degree to which the reaction follows a DHP (CO ideally absent) vs a direct ODHP (ideal CO/propylene ratio of 1) vs the indirect ODHP pathway (ideal CO/propylene ratio follows the rWGS equilibrium, which increases with T). For VO_x/Al_2O_3, it sharply increases from 0 to 1 between 400 and 450 °C and then it slowly increases from 1 (indicating an

ODHP direct pathway) to 1.7 (Figure 5 left). This increase highlights as well the increased extent of dry-reforming and coking reactions, which generate extra CO and H_2.

To contrast the behavior observed over VO_x/Al_2O_3, we consider an established catalyst, which proceeds via an indirect (O)DHP mechanism, e.g., CrO_x/Al_2O_3 (Figure 5 right). At low temperatures of <600 °C, the H_2/propylene ratio is equal to 1, suggesting a reaction pathway via the DHP reaction. The CO/propylene ratio gradually increases from 0 to 0.5 with increasing temperature due to the increased extent of the rWGS reaction (in series with DHP). At high temperatures, side reaction contributions increase, leading to further deviation from the ideal behavior.

When we calculate the thermodynamic equilibrium for the rWGS, based on instantaneous reaction conditions (T, P, and gas composition), we can also determine the reaction extent to equilibrium: λ_{rWGS} (solid line in Figure 5). The rWGS is thermodynamically and kinetically limited at $T < 500$ °C (endothermic) and explains the gradual formation of CO, proportional to T (Figure 5, right). However, for the direct mechanism catalyst (Figure 5, left), the rWGS alone could not explain the product distribution, as it would exceed thermodynamic equilibrium ($\lambda_{rWGS} > 1$), thus further validating the presence of a different reaction mechanism converting CO_2 for such materials (direct ODHP). In fact, at $T < 450$ °C, the exothermic WGS dominates, and it consumes CO and H_2O (generated by direct ODHP), which results in lower ratios of CO/propylene < 1. When temperatures are in the 450−530 °C range, this WGS extent will diminish, and direct ODHP will be dominant. A small degree of nonoxidative PDH is also present, as documented for V in DHP experiments without the CO_2 feed, which explains the rise in the H_2/propylene ratio, as well as coking, which consumes propylene to convert it into H_2 and C.

At higher P, selectivity with V remains stable, with a 1.2-fold increase in conversion achieved during the T-ramp experiment despite an increase in the partial pressure of the feed gases and 4 times longer residence time inside the reactor. At the end of both T ramps (Figure 4, first and second runs), at $T = 600$ °C and $P = 0.7−6.0$ barg, the space time yield for propylene was maximum ($STY_{propylene} = 6.2−6.5$ mol h^{-1} kg_{cat}^{-1}) and $S_{propylene}^{HC}$ was 91−87%, but the overall selectivity was poor ($S_{(O)DHP} = 65−55$%).

Coking is the dominant side reaction and the main deactivation contributor, accumulating heavy hydrocarbons on the surface of the catalyst and plugging active sites until air regeneration. We can observe such a phenomenon by monitoring the CB evolution during the reactions (Figure 4, top) and also by the 7-fold drop in conversion for both reactants during the isothermal time-on-stream (TOS) experiments at 600 °C (Figure 4). On the other hand, $S_{propylene}^{HC}$ and $S_{(O)DHP}$ improve over time, at the expense of a decline in coke formation, DRP, and cracking reactions—due to the preferential obstruction of highly active but unselective sites first. Coke forms mainly from the polymerization of adsorbed propylene,[60] and indeed, higher concentrations correlate to a faster deactivation kinetic also in our additional catalytic tests with other active metals but the same alumina support. After the final TOS (6 h), we also measured the amount of coke present on the catalyst with elemental analysis (CHN); it was found to be 12.0 wt %, which also confirms the carbon balance integration (CB: 12.5 wt %) and thermogravimetric analysis (TGA: 12.3 wt %), giving the same result. TGA indicates that 80% of the deposited carbonaceous species consist of hard coke,[61] and unfortunately, this graphitic form is more resistant to dry-reforming via the rBoudouard reaction compared to soft coke[27,62] at ODHP reaction conditions.

Additionally, it is worth mentioning that running a T ramp with a catalyst that concurrently forms coke inevitably reduces the apparent reaction rates compared to fresh catalytic activity. However, we noticed that during the T ramp, the various reaction rates (ODHP, cracking, coking, and reforming) increase faster than any deactivation phenomenon induced by the accumulation of coke—as long as the CB > 99% (which is around 550 °C for this catalyst). We corroborate this from three observations: (i) the Arrhenius plot for the various reactions—calculated with intrinsic kinetics via a first-order power-law model—shows linearity in this region (Figure 7S, $R^2 > 98$%); (ii) the resulting E_a^{coking} 230 kJ $mol^{-1} \gg E_a^{(O)DHP}$ 94 kJ mol^{-1} (Figure 8S), which indicates that the onset of the coking reaction would occur at higher T compared to (O)DHP; and (iii) if coke accumulation is small enough that it does not occlude the pores and active sites of the catalyst during the T ramp, then we measure no difference in activity between the final rates of the T ramp (at 600 °C) compared to the initial rate of the TOS (at the same conditions).

Toward the end of both isothermal TOS reactions (5−6 h), the catalyst reaches a pseudo-steady-state where side reactions are minimized, and we can measure the intrinsic catalytic activity of the material, which operates via the direct ODHP mechanism—H_2/propylene ratios are low (0.7−0.5) ($P = 0.7−6.0$ barg) and CO/propylene ratios are stable and close to unit (1.1−1.1). This suggests that, kinetically, CO_2 is capable of reoxidizing the reduced $VO_{x−1}$ species—because the product distribution matches the ODHP reactivity—but CO_2 does not reoxidize the hard coke. For these reasons, we exclude the fact that the deactivation mechanism is due to the irreversible reduction of the active material. However, partial reduction to vanadium species with the intermediate valence state might also occur (in parallel to coking) and contribute to the rapid deactivation of the catalyst at the beginning of the TOS (0−2 h). For example, in the dehydrogenation of ethylbenzene in the absence of CO_2, the oxidation state of a vanadium catalyst dropped from V^{5+} (fresh) to V^{2+} (spent). Instead, in the presence of CO_2, the spent material maintained a V^{4+} state, demonstrating the chemical potential of CO_2 to partially reoxidize V sites to an intermediate state.[63] Similarly, in our case, air regeneration at 600 °C reoxidizes the active metal presumably to the same valence state present in the fresh catalyst after air calcination at 600 °C in an oven: V^{5+}; at the beginning of our TOS, highly valent VO_x species populate the surface of the catalyst. During the first 2 h of the time on stream (TOS), we assist at a dynamic behavior; the ODHP reaction rate is the highest but also deactivates the fastest, compared to the rest of the TOS (2−5 h). We believe that initially the activity is the highest due to V^{5+} species. Subsequently, progressive accumulation of reduced V sites would then increase the probability of surface reaction with a CO_2 molecule and diminish the number of highly valent V sites responsible for fast propane dehydrogenation. Eventually (TOS > 5 h), accumulation of $VO_{x−1}$ in an intermediate valence state balances both reaction rates between oxidation and dehydrogenation ($r_{reoxidation} = r_{ODHP}$), and the catalyst reaches a pseudo-steady-state, biased only by the slower accumulation of coke.

To further validate our assumptions and the LCA model, we demonstrate the application of VO_x/Al_2O_3 mimicking Oleflex's industrial reaction conditions over 24 h of TOS at 600 °C. We increased the partial pressure of both propane and CO_2 to 47 kPa, reduced the inert dilution by a factor of 10, and decreased the GHSV by a factor of 10 while maintaining the same WHSV with respect to the screening methodology (Figure 6).
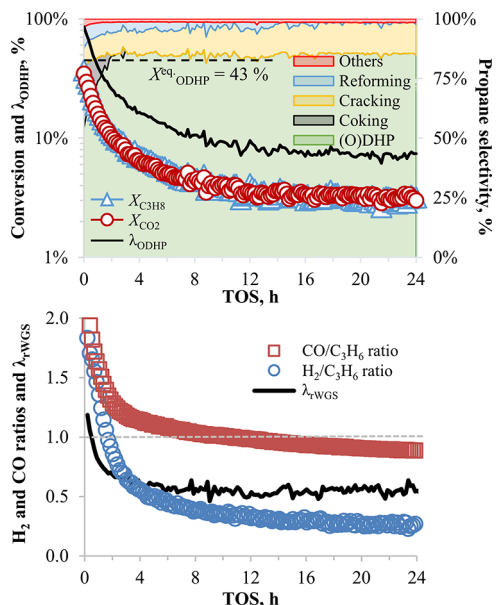

Figure 6. Isothermal 24 h TOS test with 200 mg of VO_x/Al_2O_3 at 600 °C, 0.9 barg. We allowed a flow of 10 N mL min^{-1} of gas: 25% propane, 25% CO_2, 50% N_2, GHSV = 4000 N mL mL$_{cat}$$^{-1}$ h^{-1}, WHSV = 1.5 g$_{propane}$ g$_{cat}$$^{-1}$ h^{-1}. (Top) Conversion and selectivity based on propane and considerations related to the thermodynamics of the ODHP reaction. The dashed black line represents the thermodynamic limit for the ODHP equilibrium, and the full black line is the reaction extent λ_{ODHP} relative to the conversion of propane. (Bottom) CO and H_2 to propylene ratios and the λ_{rWGS} reaction extent.

The increase in partial pressure reduces the thermodynamic equilibrium to 43% ($X_{ODHP}$$^{eq.}$ = $X_{propane}$$^{eq.}$ = $X_{CO2}$$^{eq.}$ assuming a direct mechanism, dashed horizontal line), and we can observe that at the beginning of the TOS the reaction extent λ_{ODHP} (black line) reaches almost 90% of the full extent, to drop later due to the decline in catalyst activity. The CB quantifies coking during the first 4 h of TOS, which correlates with the decline in catalyst activity and the improvement in selectivity for propylene (Figure 6 top), as well as the coproducts CO and H_2, because of the prevalence of coking and DRP side reactions (Figure 6 bottom). During this time, S_{others} drops from 4 to 1%, which includes (relative %) ethane (60 to 90% during 0−4 h of TOS), isobutylene (15 to 0%), 1-butene, c- and t-2-butene (5 to 0% each), and 1,3-butadiene, cyclopropane, and propadiene (3% each). We observe that after 12 h the catalyst reaches a pseudo-steady-state, with constant conversions and propylene STY of 1.2 mol h^{-1} kg$_{cat}$$^{-1}$, while coking and DRP become barely detectable. The CO/C_3H_6 ratio gradually drops from 1 to 0.9, indicating either conversion of CO via the WGS equilibrium or the copresence of indirect and direct (major) ODHP mechanisms. Postmortem CHN analysis quantifies 12 wt % coking on the catalyst, which, compared to the overall production of propylene and the

conversion of CO_2, corresponds roughly to a molar ratio of propylene/carbon (C from coke) and CO_2/carbon both of 21. This demonstrates that from an LCA perspective it is beneficial to run the catalyst for long TOS, as coking occurs during the first few hours, leading to improved selectivity. However, from a process intensification point of view, this is not ideal: STY (productivity) drops by half in the first hour and by a factor of 10 in 8 h. Deactivation between 12 and 24 h of TOS instead is almost null.

CrO_x, CoO_x(700), GalinstanO$_x$, and InO$_x$/Al_2O_3. We now examine thoroughly four distinct catalysts from the screening, by showing their T ramp and TOS isothermal behaviors (Figure 7 left and middle) and a T-ramp reaction under rWGS conditions (Figure 7 right). Together with VO_x/Al_2O_3 in Figure 4, the following are the most promising materials: (i) CrO_x, due to high activity; (ii) CoO_x, due to the coke-reforming capability; (iii) GalinstanO$_x$, a low-melting-point eutectic alloy of Ga$_{0.78}$, In$_{0.15}$, and Sn$_{0.07}$, which is novel to the literature and selective and stable for ODHP via a direct mechanism compared to the high-melting-point GaO$_x$; and (iv) InO$_x$, due to the high CO_2 uptake due to rWGS.

Chromium oxides catalyze propylene synthesis at 615 °C, 0.9 barg with X_{C3H8} = 48% and STY = 12 mol h^{-1} kg$_{cat}$$^{-1}$, the highest among the γ-Al_2O_3-supported catalysts (Figure 7 first row and Figure 9 "Cr"). DRP is negligible, while coking and cracking are the main side reactions: S_{coke} = 10%, $S_{cracking}$ = 7%, $S_{(O)DHP}$ = 75%, and S_{C3H6}^{HC} = 90%. The catalyst converts twice as much propane than CO_2 (X_{C3H8} = 48% vs X_{CO2} = 23%, Figure 1 right), following an indirect mechanism: CrO_x dehydrogenates propane (H_2/propylene ratio remains constant at 1.0), and in series, the rWGS converts H_2 to CO (the CO/propylene ratio gradually increases from 0.1 to 0.5, Figure 5 right).

Up to 550 °C, the reaction is the most selective, while from 550 to 700 °C, coke formation consumes propylene to generate extra H_2 that shifts the ratios to higher values. In fact, in this range, we reach a maximum in conversion at 615 °C, followed by a drop in activity ostensibly due to coke obstructing the active sites (confirmed by the CB and measurement after the TOS at 600 °C: TGA: 1 wt % soft coke, 3 wt % hard coke; and CHN: 4 wt % carbon). When we integrate the amount of propylene synthesized and compare it with the amount of carbon (coke) deposited during the TOS, we obtain a molar ratio of 7 mol of propylene synthesized per mole of C coked on the catalyst. When we consider the consumption of moles of CO_2 per mole of C coked, we get a ratio of 3. The catalyst at this stage was still reasonably active and could have been used for a longer TOS, but considering regeneration at this stage, the net CO_2 input−output in our LCA flow would be 30% lower and thus GHG would be 10% higher compared to ideal conditions.

Coke deposition is the main factor responsible for the reversible deactivation observed; however, we believe that sintering causes a sharp drop in activity observed during the T ramp at 650−700 °C (max T of both T ramps). In fact, we fail to regain the same activity during the TOS (Figure 7 TOS rates are shifted downward compared to the T ramp), and the calculated pre-exponential factors score lower during the second T ramp at 6 barg, which we believe correlates with a lower number of accessible active sites (Table 4S). At the same time, activation energies increase, which we believe is the result of morphological changes in the sintered active material. Experiments at 6 barg (Figure 15S) also lowered selectivity
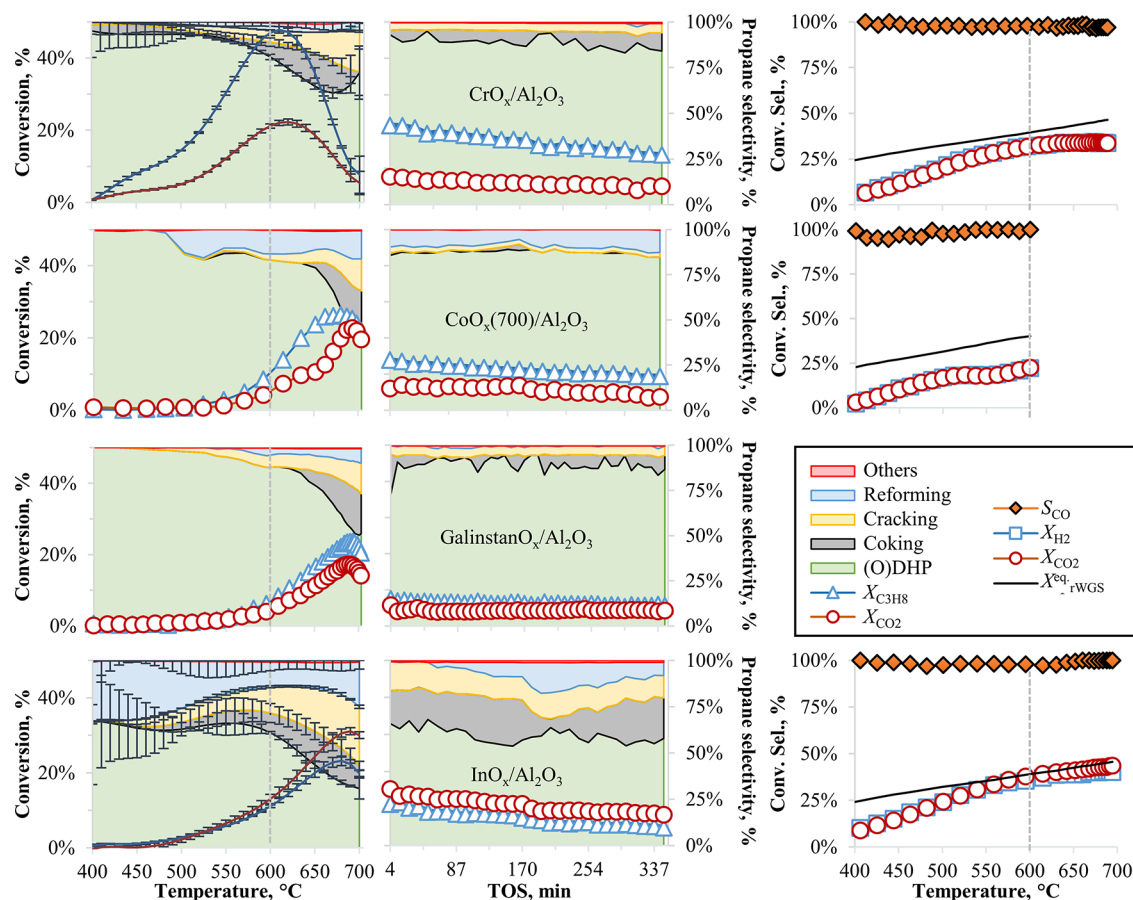
Figure 7. CrO_x, $CoO_x(700)$, $GalinstanO_x$, and InO_x/Al_2O_3 (top to bottom) tested during the T ramp at 0.9 barg (first column); the isothermal test at 600 °C, 0.9 barg over 350 min (second column); and the rWGS reaction (third column); we exchanged the propane gas for H_2 under the same experimental procedure, and we report the equilibrium line of eq 3 ($X_{rWGS}^{eq.}$). To compare data at the same temperature and to calculate error bars at 1 $\delta_{n=2}$, a sixth-order polynomial fits the raw data from two repeated tests for Cr and In. The third row reports also the legend (additional plots are provided in the SI).

($S_{(O)DHP}$ = 65% and S_{C3H6}^{HC} = 85%), which is a common trend among all catalytic materials independent of sintering, and we believe it is due to the more difficult propylene desorption at higher P (due to thermodynamic equilibrium). This results in a higher concentration of adsorbed propylene species, longer residence time of the said species, and therefore, consecutive surface reactions of the adsorbed propylene to coke and dry-reforming products.

For these selected catalysts, we also studied them under rWGS conditions (Figure 7, right) since this is the main mechanism of CO_2 conversion for indirect mechanism materials. In particular, for CrO_x, $X_{CO2,H2}$ = 33%, the reaction approaches equilibrium with a reaction extent λ_{rWGS} = 60% (at 600 °C, 0.6 barg). In comparison, during ODHP, X_{CO2} = 23% is lower. Two reasons can explain this situation. (i) Because H_2 concentration relates to propylene synthesis and is limiting, we have a lower conversion for CO_2. However, (ii) when we calculate the thermodynamic equilibrium at the reaction conditions λ_{rWGS} = 30%, it indicates that the H_2 concentration is not limiting, but the rWGS reaction is slower in the presence of propane. This might indicate different activation pathways or competitive kinetics of CO_2 and propane for the same active site. Further evidence for that is found in a significant difference between CO_2 activation under rWGS and ODHP (Table 4S): under rWGS, E_a^{CO2} is 62(2) kJ mol^{-1} and is invariant between low and high pressures, while under ODHP,

E_a^{CO2} is 78(2) kJ mol^{-1} at low P and 97(1) kJ mol^{-1} at high P. We can also observe that during rWGS, the material shows the same activity between T ramp and TOS (at 600 °C, Figure 16S left and right)—absence of irreversible deactivation, unlike in the case of the ODHP reaction—which indicates that ODHP conditions are more severe for catalyst stability. Moreover, during the TOS for the rWGS experiment, the catalyst activity drops over time, probably due to reduction of the Cr centers (as a side reaction in a reducing environment), since coke is absent (CB) and CO_2 is unable to reoxidize the active site to the highly valent Cr^{6+} species (Figure 16S right).

As is known that metallic Co can catalyze the reverse Boudouard reaction,[64] we tested cobalt oxide under ODHP to determine if Co would follow a redox mechanism and react with CO_2 to consume coke, ideally while maintaining stable reactivity. CoO is the prevalent oxide form when calcining the salt precursors in air at 600 °C, while Co_2O_3 forms at temperatures between 600 and 700 °C. At 800 °C, Co reacts with Al_2O_3 to form $CoAl_2O_4$, a similar crystal structure that also occurs when Cr is exposed to excessive temperatures, irreversibly deactivating the metal oxide. We first reacted the catalyst calcined in air at 600 °C—Co(600) in Figure 9, limiting the T-ramp test to 600 °C (Figure 17S-a). We then calcined in situ the same catalyst at 700 °C in air for 4 h—Co(700)—and collected the additional temperature ramps (up to 700 °C this time, Figures 7 and 17S-b). As the third sample,

we calcined the material in air at 800 °C and obtained the Co—Al-sintered material—Co(800); see Figure 17S-c.

Calcination at the lowest temperature proved to be the best procedure, which is realized during the T ramp at 600 °C, 0.9 barg, and STY = 4.7(1) mol h^{-1} kg$_{cat}$$^{-1}$ with low coke deposited (1(1) %, from CB, 80 wt % hard coke—TGA) and high propylene selectivity S^{HC} = 96.3(1)%. DRP is the main side reaction that consumes propane. Co appears to occupy the Al$_2$O$_3$ Brønsted acid sites, as evidenced by the minimized cracking and coking side reactions compared to the blank test (Al$_2$O$_3$—Figure 10S). The difference between X_{C3H8}, X_{CO2}, and the rate of formation of H$_2$ and CO points to an indirect mechanism similar to that of Cr. During the rWGS reaction, Co approaches equilibrium at λ_{rWGS} = 60% at low P, similar to that in the case of Cr, and λ_{rWGS} = 90% at 600 °C and 6 barg. However, the conversion curves show a sigmoidal behavior over the range of temperatures studied, with two peaks at 520 and 608 °C (Figure 7).

Increasing the calcination and reaction temperatures above 600 °C leads to progressively lower STY and increased coke formation (Figure 9). For Co(700), during the T ramp at 600 °C, 0.9 barg STY drops to 3.2 and 2.0 mol h^{-1} kg$_{cat}$$^{-1}$ for Co(800), while that for coke increased: 14 and 11% (CB) or 13 and 10% (CHN). However, for Co(700) and Co(800), propane conversion remains stable between 650 and 700 °C, while CO$_2$ conversion has two characteristic bumps at 630 and 690 °C, similar to that during rWGS, which might indicate activation of the rBoudouard reaction at higher temperatures (Figure 17S-c). In fact, in the last portion of the T ramp T > 680 °C, we can observe how CO$_2$ conversion rapidly increases, eventually matching propane's.

When we tested a CoO$_x$ catalyst, promoted with potassium (1.08−0.22 mmol of M g$_{Al2O3}$$^{-1}$: Co5-K in Figure 9), we observed improved selectivity at the expense of a decline in activity: S_{C3H6}^{HC} = 99% and STY = 2.7 mol h^{-1} kg$_{cat}$$^{-1}$ (T ramp at 600 °C, 0.9 barg). Potassium saturates the Bronsted acid sites of the support, minimizing coking (below detection via CB) and cracking side reactions. If that is the case, then sequentially impregnating the active metal first, and the alkali dopant later, might result in an even better dispersion of the active metal (avoid the decline in activity, as Co and K might compete for the same grafting sites during coimpregnation and calcination). Moreover, surface acidity titration of the calcined supported active metal oxide would give a precise measurement for the dose of alkali dopant required to saturate the free acid sites present on the catalyst. During the isothermal TOS, this catalyst showed the lowest deactivation rate for propane and an actual improvement in CO$_2$ conversion over time, further validating rBoudouard capabilities for this material (Figure 9 top).

Gallium oxide (Figure 22S) follows a similar behavior with respect to Cr and Co, converting more propane than CO$_2$. At 600 °C and 0.9 barg, X_{C3H8} = 28% and X_{CO2} = 9% and the maximum conversion is for X_{C3H8} = 39% at 650 °C, after which it rapidly drops. Likewise, the H$_2$/propylene ratio remains constant at 1.2 at low temperatures, while the CO/propylene ratio gradually increases from 0.3 to 0.6 at 600 °C due to rWGS, indicating that the indirect mechanism is at play. The material maintains an S_{C3H6}^{HC} > 95% up to 600 °C, reaching an STY of 7.8 mol h^{-1} kg$_{cat}$$^{-1}$; then, cracking causes this value to drop at higher temperatures. We noticed this common trend in all of our catalytic screenings. The alumina support activates above 650 °C, shifting the product distribution toward

cracking, due to surface acidity. In this temperature region, coking is also prominent and deactivates the catalyst similar to that of CrO$_x$. After the T ramp at high P (Figure 22S right), the GaO$_x$ catalyst accumulated a similar amount of coke compared to CrO$_x$ under the same reaction conditions (CHN: 14 vs 13%). Also, similar to CrO$_x$, the GaO$_x$ catalyst had less activity compared to the ramp at low P, indicating a partial irreversible deactivation, which we believe is caused either by sintering or by volatilization of the active metal, as also suggested by the TPR experiments for Galinstan. Likewise, under rWGS conditions (Figure 23S), the catalyst behaves similarly with respect to CrO$_x$, approaching equilibrium at low pressures and reaching thermodynamic equilibrium at 600 °C, 6 barg, due to the longer residence time in the reactor. However, GaO$_x$ better approaches equilibrium under rWGS and maintains a stable reactivity during the isothermal test compared to CrO$_x$, which during the T ramp between 600 and 700 °C sees a plateau in conversion (Figure 16S left). We think this phenomenon is due to the absence of redox mechanisms for Ga, as reported in the literature.[4]

Galinstan is a eutectic alloy of Ga, In, and Sn (1.02−0.19−0.09 mmol of M g$_{Al2O3}$$^{-1}$) that is liquid at room temperature, which was supported using alumina and calcined in air to obtain Galinstan oxides. At 600 °C, despite the catalyst composition being mostly Ga (>80%), STY = 2.5 mol h^{-1} kg$_{cat}$$^{-1}$ and X_{C3H8} = 8.3% are modest compared to those of pure GaO$_x$, which is 3 times more active. This indicates the absence of phase segregation—that would have shown activities proportional to the loading of Ga and In—and we can assume that the catalytic behavior is due to the metal oxide alloy. In turn, GalinstanO$_x$ activates CO$_2$ in a greater proportion compared to pure GaO$_x$ (X_{CO2} = 5.6% at 0.9 barg), with a product distribution similar to a direct mechanism catalyst (Figure 5 left) with a low H$_2$/propylene ratio (0.2−0.5) and a higher CO/propylene ratio (0.3−0.8) that gradually increases up to 600 °C. At P = 6 barg, the ratios are even closer to that required to follow a direct mechanism—possibly due to catalyst activation after the first T-ramp reaction−regeneration cycle—with H$_2$/propylene = 0.1−0.5 and CO/propylene = 0.8−1.3. Furthermore, cracking, DRP, and coking consume 20% of the feed propane. During the 6 barg isothermal TOS, the catalyst accumulates coke of 5 wt % (CHN), composed of 60% hard coke (TGA), but this does not cause the activity to drop. Galinstan is one of the catalysts with the most steady-state conversion rate and the lowest deactivation constant at high P (Figure 9S), maintaining X for both gases at around 6% and S_{C3H6}^{HC} of 89%. Under ODHP conditions, GalinstanO$_x$ remained active throughout two T ramps up to 700 °C and the two TOS, in contrast to the volatilization phenomenon that occurred during H$_2$-TPR, indicating that CO$_2$ is capable of reoxidizing the active sites.

Finally, indium oxide on alumina exhibits an interesting catalytic behavior with a higher CO$_2$ conversion compared to propane (Figure 7), suggesting not only a dominant direct catalytic mechanism but also a DRP side reaction, which consumes 3 moles of CO$_2$ per mole of propane (eq 6, Table 2). When dispersed on SiO$_2$ gel, the metal oxide showed no reactivity, while on ZrO$_2$, it showed an even higher reforming selectivity (S_{DRP} = 40%, Figure 9).

Similar to other direct mechanism catalysts (Figure 5, left), InO$_x$/Al$_2$O$_3$ has CO/propylene ratios greater than H$_2$/propylene. However, DRP and coking shift such ratios to higher values because of the production of extra H$_2$ and CO
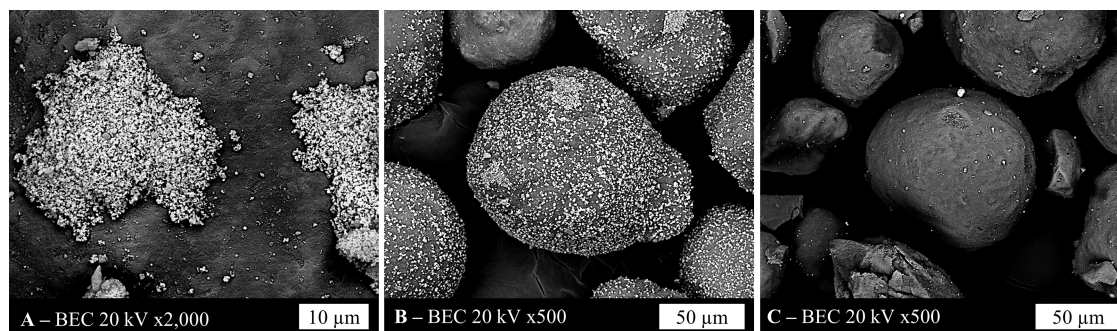
Figure 8. Backscattered electrons (BECs) scanning electron microscopy (SEM) morphology of external In_2O_3 NPs (white submicron particles) on Al_2O_3 (100 μm spheres). (A) Calcined fresh InO_x/Al_2O_3 catalyst agglomerates In_2O_3 NPs in 30 μm clusters on the Al_2O_3 support (dark background). (B) After several reaction−regeneration cycles, the spent catalyst disperses the clusters of NPs all over the external surface. (C) After the rWGS reaction, the external NPs disappear and are incorporated in the porosity of the support.

(Table 2, eqs 6−7). During the first T ramp at low P—and between 500 and 600 °C—the catalyst is the most selective for propylene: $S_{C3H6}^{HC} > 80\%$ and $S_{C3H6} > 65\%$. In this range, the H_2/propylene ratio increases from 0.3 to 0.9 (at 600 °C), while the CO/propylene ratio remains constant around 2, approaching rWGS equilibrium: $\lambda_{rWGS} = 40−80\%$ (Figures 18S−19S). Propylene selectivity rapidly drops between 600 and 700 °C, reaching a maximum at 650 °C with STY = 2.9 mol h^{-1} kg$_{cat}$$^{-1}$ at 0.9 barg and STY = 4.5 mol h^{-1} kg$_{cat}$$^{-1}$ at 6 barg, with $S_{C3H6}^{HC} \approx 65\%$ and $S_{C3H6} \approx 50\%$ in both cases. Coke forms and is mostly graphitic (70%, TGA after the TOS), but it does not deactivate the catalyst until 670 °C, and we believe this is the only cause for deactivation, unlike for CrO_x, where the catalysts rapidly loses 80% of the activity between 600 and 700 °C. Deactivation is reversible, and air calcination at 700 °C removes the carbonaceous deposits, actually increasing the X_{C3H8} (T ramp at 600 °C) from 11% (0.9 barg) to 16% (6 barg) and the X_{CO2} from 13 to 16%. Conversion remains the same during the T ramp at 600 °C, 0.9 barg, and the TOS was $X_{C3H8} = 11\%$ and $X_{CO2} = 14\%$, which indicates the cyclable behavior of the catalyst. Only the reforming side reaction drops, arguably by better redistribution of the active metal on the surface of the support, after the reaction−regeneration cycles (Figure 8A,B and additional in the SI).

We initially noticed this redistribution effect when reducing chromium oxides with H_2, followed by air regeneration. Metallic Cr^0 and Cr_2O_3 have Tamman temperatures above 800 °C and are stable upon heating. CrO, CrO_2, CrO_3, and polymeric Cr^{+6} grafted on Al_2O_3, on the other hand, have melting temperatures below 400 °C, and the likely bulk atom mobility and higher surface energy allow for migration and redistribution of these species under reaction conditions, resulting in a higher propane reaction rate (Figure 14S). The SEM morphologies of CrO_x/Al_2O_3 and VO_x/Al_2O_3, before and after both ODHP and rWGS reactions, do not change (Figures 35S−37S). The support pores host most of the active metal oxides, with only a few nanoparticles (NPs) visible on the external surface (<0.5 wt %, geometrical estimation based on the average number of NPs and the size and density of MO_x per particle of alumina), and we cannot appreciate any morphological variation. Coke is also not visible, and we assume it forms in the porosity of the support, rather than on the surface of external NP metal oxides.[65]

In the case of InO_x/Al_2O_3, the fresh material after calcination appears to have a greater portion of active metal oxides, in clusters of NPs of In_2O_3, segregated from the parent alumina support, which we could quantify (SEM on the SI) as roughly 50 wt % external In_2O_3 NPs (Figures 8A and 38S−39S). However, this morphology changes when exposed to different reaction gases. After the test under ODHP screening conditions, the NPs appear dispersed on the surface (Figure 8B), without any appreciable change in the NP size (submicron Figure 8A,B). This supports the hypothesis that In_2O_3 (T_{Tamman} = 820 °C) partially reduces at the interface to metallic In^0 (T_{Tamman} = −58 °C), which in turn becomes mobile and reoxidizes with CO_2 in different spots on the alumina support, thus homogeneously spreading across the external area of the support (Figure 39S). However, the size of the NPs probably depends on the interaction between the support and the surface tension of the metallic interface. A similar behavior was also observed in boron oxide/hydroxide supported catalysts for O_2-ODHP (T_{Tamman} = −52/89 °C), where the active material became mobile during thermal treatment and clustered.[66]

More interestingly, the rWGS reaction (same conditions as ODHP experiments, but H_2 in place of propane) helped eliminate the external NPs, redistributing the materials in the pores of the support (Figures 8C and 40S). The TOS experiment shows stability without any occurrence of deactivation phenomena, and the reaction data collected during the first T ramp at 600 °C, 0.9 barg, coincide with the activity recorded during the TOS under the same conditions (tested after two cycles of T ramps up to 700 °C interleaved by air regeneration) (Figures 7 and 19S). For these reasons, we exclude the possibility that the material volatilized or coated the internal walls of the reactor tube since those phenomena are time-dependent and cycle-dependent. Bulk In_2O_3 NPs and supported on CeO_2 are known catalysts that promote CO_2 hydrogenation for rWGS and MeOH synthesis.[67−69] However, to our best knowledge, no examples in the literature have been reported of InO_x/Al_2O_3 systems with such remarkable CO_2 activation features. During the rWGS T ramp at 500 °C, 0.9 barg, $X = 24\%$ (for both CO_2 and H_2) and $STY_{CO} = 7.6$ mol h^{-1} kg$_{cat}$$^{-1}$ (however, the kinetic here is biased due to approaching equilibrium: $\lambda_{rWGS} = 75\%$). At 600 °C, $\lambda_{rWGS} = 98\%$, $X = 37\%$, and $STY_{CO} = 11.6$ mol h^{-1} kg$_{cat}$$^{-1}$. At 6 barg, the data is substantially the same because we already reached equilibrium at 450 °C. Remarkably, during the TOS at 600 °C, 0.9 barg, $S_{CO} \approx 100\%$ (no other product is detected by GC-FID-TCD and coke deposit is close to zero: CB = 0%, CHN = 0.2 wt %) and also deactivation (k_d) is zero. By the Arrhenius linear regression on the T ramps (between 270 and
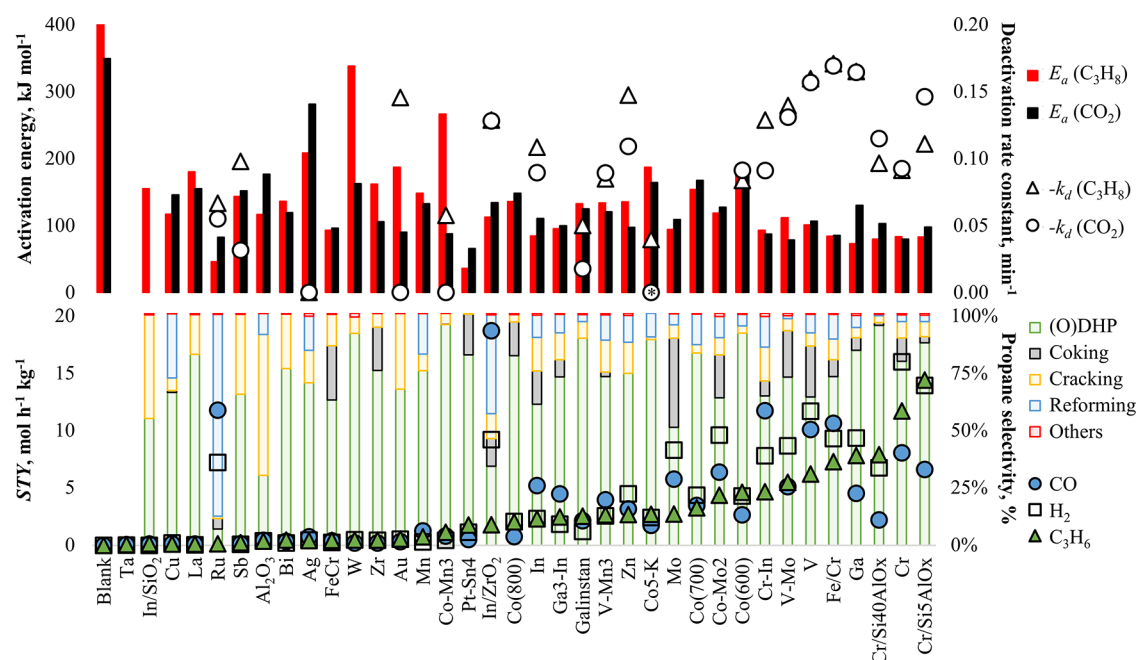
Figure 9. On the top, propane and CO_2 activation energies assuming a first-order power law and differential conditions (bars) during the T ramp and their deactivation rate (symbols) during the isothermal reaction at 600 °C, 0.9 barg (data at 6.0 barg and at maximum STY in the SI). *Co_5-K increases the CO_2 uptake over time ($-k_d = -0.16$ min^{-1}) arguably due to K_2CO_3 formation. At the bottom, we list the same catalysts (active metal supported on Al_2O_3 if not specified) from the least active (left), reporting the reaction selectivity (bars) and the STY for propylene, H_2, and CO (symbols), at 600 °C, 0.9 barg, during the same T ramp.

350 °C, λ_{rWGS} = 3–17%), we calculate an E_a of 90 kJ mol^{-1} (Figure 20S, Table 5S), which is a remarkable result compared to high-temperature Fe–Cr catalysts[70] and Fe/Al_2O_3 catalysts.[71] It mounts to a reduction in the activation energy (Fe–Cr catalysts: E_a = 95–120 kJ mol^{-1}) and increase in the reaction rate (Fe/Al_2O_3 catalysts: approaches CO_2 conversion to equilibrium conditions λ_{rWGS}: 70% at 600 °C and GHSV = 12 000 mL g_{cat}^{-1} h^{-1} with H_2/CO_2 ratio of 4:1 vs reached equilibrium at 600 °C at GHSV = 30 000 mL g_{cat}^{-1} h^{-1} with a H_2/CO_2 ratio of 1:1 in this study).

Following the same approach, we discuss the performance of the other screened catalysts, from the least active toward (O)DHP to the most, looking at the reaction activity, selectivity, as well as stability (Figures 9 and S24–S33).

From the left to right in Figure 9, we find the low-activity catalysts: Au, Ag, ZrO_x, WO_x, SbO_x, LaO_x, and TaO_x /Al_2O_3. The materials were tested at low and high pressures (6 barg), without substantial differences from the reactivity of bare alumina at the same conditions. Significant differences arise in the amount of coke deposited: Al_2O_3 = 2.1(2) wt %, WO_x = 5.6 wt %, (CHN analysis), Au = 4 wt %, Ag = 6 wt %, ZrO_x = 0 wt %, SbO_x = 2 wt %, LaO_x = 0 wt %, TaO_x = 0 wt % (CB estimation), and conversions (Figure 33S). W, Sb, La, and Ta oxides occupy the alumina sites and inhibit propane reactivity. Au, Ag, Zr, and W appear to convert more propane than CO_2; Sb, La, and Ta convert similar amounts of propane and CO_2.

CuO_x/Al_2O_3. A Cu–Al bimetallic oxide "sponge" was reported to outperform noble metal catalysts in DHP.[72] When we tested this active metal on alumina for ODHP however, we found low activity; the STY was low (0.3 mol h^{-1} kg_{cat}^{-1}) (Figure 9 bottom). To increase productivity in the reactor and raise product detection, we loaded 2.8 g of catalyst (vs the standard 0.2 g). No reactivity was measured below 500 °C; the material thus required higher temperatures to activate

the reactants ($E_a^{propane}$ = 120 kJ mol^{-1}; E_a^{CO2} = 150 kJ mol^{-1}; Figure 9 top). Concurrently, coking and reforming consumed most of the propane, thus increasing CO_2 consumption. The reaction pathway appears to be indirect (H_2/propylene > 2), and the catalyst irreversibly deactivated at 700 °C, arguably due to sintering.[73] Indeed, copper is not suitable to work at T > 300 °C, and the propylene selectivity dropped by half during the ramp at 6 barg.

RuO_x/Al_2O_3. Ruthenium oxides efficiently catalyze the DRP reaction, consuming CO_2 and propane in a stoichiometric amount (3:1). Propylene is absent below 550 °C, either because Ru does not catalyze DHP or because propylene is also rapidly consumed by CO_2 via dry-reforming (STY < 0.2 mol h^{-1} kg_{cat}^{-1}). At higher temperatures, CO_2 becomes the limiting reagent and we detect propylene (Figure 32S). We can observe a drop in conversion at high pressures due to irreversible deactivation after the first ramp at 700 °C and air calcination. Simultaneously, the cracking side reaction becomes prominent, and we can hypothesize that after the first T ramp the active material sintered, agglomerated, and exposed a fresh Al_2O_3 surface to catalyze propane cracking.

BiO_x/Al_2O_3. Bismuth oxide appears to catalyze ODHP via a direct mechanism, converting CO_2 and propane in equal amounts based on the H_2/propylene and CO/propylene ratios. The catalytic activity is low (STY = 0.4 mol h^{-1} kg_{cat}^{-1} at 600 °C) but selective. At the highest STY of 2 mol h^{-1} kg_{cat}^{-1} (690 °C, 0.9 barg), coking and cracking severely disrupt selectivity (50%). Interestingly, BiO_x is one of the few active metals (with Ag, Au, Co-Mn_3, and Co_5-K, where the subscripts denote the molar ratio) that increases in activity during the isothermal TOS reaction (Figure 29S). For this reason, we hypothesize that BiO_x is capable of dry-reforming coke via the rBoudouard reaction.

MnO_x/Al_2O_3. Manganese oxide follows a similar reactivity as BiO_x, via a direct mechanism, converting CO_2 and propane in equal amounts. The H_2/propylene ratio increases from 0.3 to 3 and the CO/propylene ratio averages around 2 over the entire temperature range, with similar ratios at high pressures (Figure 30S). The Mn activity is higher than Bi, and it is less prone to coking, reaching an STY of 0.8 mol h^{-1} kg_{cat}^{-1} at 600 °C. In comparison, after the second T ramp, the Bi catalyst accumulated 12% coke (CB), while Mn accumulated 10% (CB, CHN). This catalyst activates at higher temperatures, and the highest yield occurs at 690 °C, 0.8–6 barg (STY = 2.6–4.3 mol h^{-1} kg_{cat}^{-1}), with DRP being the main side reaction (Figures 6S and 30S).

Pt/Al_2O_3 and PtSn_4/Al_2O_3. We tested a reference commercial Pt catalyst from Sigma-Aldrich (0.5 wt % Pt/ Al_2O_3) and also made a coimpregnated one with 0.26 mmol of Pt and 1.04 mmol of Sn per g of support (5 wt % Pt, mimicking the formulation for commercial PDH catalysts, Figure 28S). At a low loading of Pt, the acid sites of the bare support strongly influence selectivity, and cracking reactions consume 25% of the feed propane. When the activity was low, STY = 0.5 mol h^{-1} kg_{cat}^{-1}, and coke forms and accumulates on the catalyst (CHN: 4%). Increasing the loading on the Pt–Sn alloy saturates the alumina sites responsible for cracking, and this side reaction is minimized, with $S_{propylene}^{HC}$ reaching 99% at 430 °C. At this temperature, we find the maximum STY of propylene = 1.8 mol h^{-1} kg_{cat}^{-1} (at P = 0.9 barg), with $X_{propane}$ = 6% and X_{CO2} = 2%. Because H_2/propylene = 0.7 and CO/ propylene = 0.2 up to 430 °C, we can conclude that the catalyst follows an indirect mechanism. CO forms via rWGS consuming H_2, while cracking and coking are absent at low temperatures. $PtSn_4$ has the highest S^{HC} and the lowest coke accumulation among the surveyed catalysts (CHN = 0.2%, despite reacting at 600 °C during the isothermal TOS). Reaction temperatures during the T ramp reached 700 °C, which proved detrimental for the active metal, which we believe sintered because the STY halved during the subsequent T ramp at 6 barg: 0.9 mol h^{-1} kg_{cat}^{-1}. As a side note, supported Pt catalysts often require activation in a H_2 atmosphere prior to reaction. We also tried to activate the catalyst with H_2 at 600 °C, 6 barg, but the resulting activity and selectivity were similar compared to the material activated with the feed gas ramping from r.t. (standard procedure).

ZnO/Al_2O_3. Zinc oxide catalyzes propylene synthesis via indirect DHP and rWGS mechanisms. After an initial induction period (up to 580 °C at 1 barg and 660 °C at 6 barg), where propane and CO_2 are consumed in equal proportions (due to the extra CO_2 uptake from the DRP side reaction), $X_{propane}$ reaches 15% and X_{CO2} reaches 9% at 650 °C. At this temperature, we find the highest propylene yield Y = 10% and STY = 3.4 mol h^{-1} kg_{cat}^{-1}. The catalyst generates H_2/propylene = 1.7 and CO/propylene = 1.2 in constant ratios up to 650 °C; then, coking shifts the H_2 ratio to higher values.

MoO_x/Al_2O_3. Molybdenum oxide also shows a similar reaction selectivity compared to BiO_x and MnO_x, although it is more active at lower temperatures (STY = 2.8 mol h^{-1} kg_{cat}^{-1} at 600 °C) and more prone to coking reaction. At low pressures, propane and CO_2 convert at the same rate, while at high pressures, we observe a divergence starting at 650 °C, which is similar for Bi as well, due to the influence of the support, which converts more propane rather than CO_2 (Figure 31S).

FeCrO_x/Al_2O_3. Since CrO_x catalysis proceeds via an indirect pathway, we decided to promote CO_2 activation by coimpregnating 1 molar equiv of FeO_x, a well-known high-temperature rWGS catalyst. We first attempted to coimpregnate simultaneously both active metal salts (FeCr, Figure 9), followed by air calcination. This resulted in a material with poor ODHP characteristics. Improving the catalytic activity required impregnating Fe salt on a precalcined CrO_x/Al_2O_3 powder (Fe/Cr, Figure 9). We believe that coimpregnation created a homogeneous alloy of Fe–Cr oxides, which are less active and less selective. Such a catalyst was characterized by greater DRP and coking behavior (Figure 24S–25S), as suggested by the much larger proportion of CB attributed to coke (21 vs 10 wt % for the alloyed FeCr catalyst compared to the Fe/Cr catalyst). We believe that the alloyed FeCr catalyst has stronger adsorption characteristics for propylene, which in turn favors coking and reforming due to the presence of this hydrocarbon pool on the surface of the material. The greater activity of sequentially impregnated Fe/CrO_x/Al_2O_3 is ostensibly due to the segregated FeO_x and CrO_x species, which would keep their respective pathways active and selective. At 600 °C, 6 barg, this catalyst converted less propane compared to the pure Cr material: X_{C3H8} = 32% (FeCrO_x) vs 40% (CrO$_x$)—arguably due to partial Cr sites' occlusion from Fe—but more CO_2: X_{CO2} = 26% (FeCrO_x) vs 23% (CrO$_x$)—achieving the expected result. Hydrocarbon selectivity reduces due to more cracking products (S_{C3H6}^{HC} = 78% vs 85%), but the overall selectivity still favors propylene formation. DRP reactivity is the same in both cases, and the catalyst enables propane activation at higher temperatures.

For CrO_x, we also tried several supports to investigate the relation between active metal oxide dispersion and surface acidity during ODHP. SiO_2 gel (SSA = 480 m^2 g^{-1}) is a better support with respect to γ-Al_2O_3 (SASOL, SCCa-5/200) for CrO_x.[24] When we loaded 0.33 mmol of Cr $g_{SiO2gel}^{-1}$, we obtained the highest turnover frequency (TOF) of this study for chromium ($TOF_{propane}$ = 23 mol_{C3H8} mol_{Cr}^{-1} h^{-1} assuming complete dispersion of the active metal); however, the $STY_{propylene}$ was 7.5 mol h^{-1} kg_{cat}^{-1}, and the catalyst maintained similar activity among three catalytic cycles without any irreversible deactivation phenomena (Figure 13S). We also noticed that the activity improved after a H_2-activation and air-calcination treatment, as a result of arguably better dispersion of the active metal oxide. Instead, only a H_2-activation treatment (without air-reoxidation) reduced the Cr oxide species and the catalyst was less active (Figure 13S).

With the same loading, we also tested the effect of surface acidity of the support against the ODHP reaction during four reaction–regeneration isothermal catalytic TOS cycles of 200 min at 550 °C and 0.9 barg. Cr impregnated and calcined on basic γ-Al_2O_3 (pH 9.9(5)—supplier's analysis when the powders are mixed in a 10% slurry with water) resulted in lower activity (X_{C3H8} = 7%, X_{CO2} = 4% at TOS = 200 min) than the neutral and acidic ones (X_{C3H8} = 10%, X_{CO2} = 5%), despite the three having the same selectivity (S_{C3H6}^{HC} = 95%). CO_2 conversion was also found to be dependent on the reaction cycle, as it seems that the first cycle contributed to activating the material. Neutral alumina, pH 7.5(3), failed to maintain a cyclable behavior as the activity and selectivity dropped (X_{C3H8} from 10 to 5%, while X_{CO2} remained constant). Acidic alumina, pH 4.4(2), proved to be the most active, stable, and cyclable among the tested aluminas. Despite different surface acidities, CO_2 conversions remained roughly
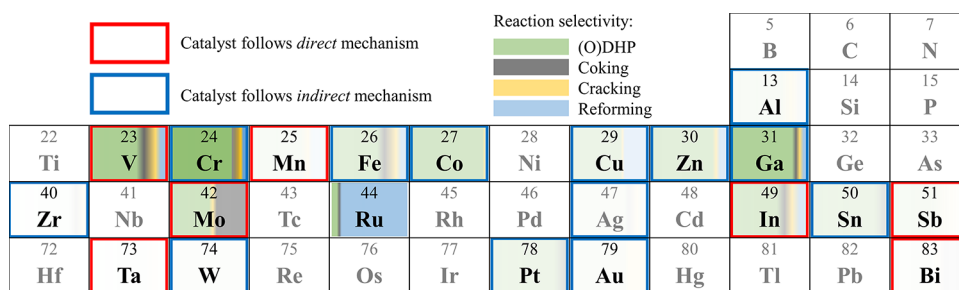
Figure 10. Investigated active elements in CO_2-(O)DHP. Color saturation is proportional to propane conversion. The green area corresponds to propylene selectivity via the ODHP or DHP reaction, the gray to coking, yellow to cracking, and blue to reforming. The cell outline represents the main reaction mechanism: red is direct (ODHP) and blue is indirect (DHP + rWGS). Data obtained at 600 °C, 0.9 barg, while ramping up in temperature. Individual analysis for each metal under the SI.

invariant. This indicates that the acidity of the support did not participate in the activation of CO_2 when Cr was used as the active metal oxide. We speculate that the different activity and stability arises from the better dispersion and grafting of Cr oxides on the surface, where the acidic alumina showed the best result.

Lewis-acidic alumina with 5% SiO_2 content (SASOL SIRALOX 5/320, specific surface area or SSA = 320 m² g⁻¹) proved to be a better support for CrO_x than pure alumina (now loaded with the common 1.3 mmol of Cr g$_{support}$⁻¹). During the T ramp at 613 °C, 0.9 barg, we obtained the highest activity for propane: X_{C3H8} = 53%, X_{CO2} = 17%, and STY = 14.7 mol h⁻¹ kg$_{cat}$⁻¹, with similar hydrocarbon selectivity but a lower coke formation: $S_{(O)DHP}$ = 85% and S_{C3H6}^{HC} = 91% (Figure 9, Cr/Si5AlO$_x$). Instead, a Bronsted-acidic alumina with 40% SiO_2 content (SIRALOX 40/480 MPV, SSA = 480 m² g⁻¹), despite the greater SSA, halved the conversion rate and STY of the catalyst (Figure 9, Cr/Si40AlO$_x$). However, both SiO_2-containing aluminas dropped in conversion but not in selectivity during the subsequent T ramp at 6 barg, also due to the irreversible deactivation at 700 °C via sintering.

Comparative Overview of Several Active Metals on Al_2O_3. We could not find correlations between the catalyst mechanism (direct vs indirect) and the properties of periodic table elements, i.e., electronegativity, hard, and soft acid–base theory or oxidizing power. To a degree, elements with lower electronegativity (1.6–1.9 Pauling scale; V, Cr, In, Ga, Co) seem to correlate with higher (O)DHP reactivity (Figure 10, green-color saturation more intense).

For certain indirect mechanism catalysts, a H-assisted pathway activates CO_2 when H atoms are dissociated on the surface of the active site via intermediate formate HCOO or carboxyl HOCO species, ultimately forming rWGS products.[4] For direct mechanism catalysts, propane dehydrogenation progresses on a limited number of highly valent metal oxide centers, in which lattice oxygen initiates the reaction by coordinating propane and abstracting H via an MvK mechanism.[39] This process ultimately desorbs water and propylene, creating an oxygen vacancy. CO_2 reoxidation on such vacancies via dissociative chemisorption to CO seems to be the dominant mechanism for redox materials, as the vacancy lowers the dissociation energy barrier even further with respect to the H-assisted pathway.[74,75]

In this context, lattice oxygen mobility becomes a discriminant factor in catalytic activity and the Tamman temperature (T_{Tamman}) qualitatively measures this effect.[37] T_{Tamman} is empirically defined as half the melting point (m.p.,

K) of a material, which is used to approximate the point at which the bulk mobility of the atoms begins to occur.[76] We assign the most stable thermodynamic form of the metal/metal oxide based on the literature or the standard electrode potential in their absence. For example, Cr_2O_3 is the most stable thermodynamic form among chromium oxides at the reaction temperature (at standard conditions, the electron potential is $E°$ = −0.74 V). Cr^{+2}, Cr^{+4}, and Cr^{+6} have T_{Tamman} < 50 °C but are unstable and will decompose upon heating (likewise for Pt, Au, and Ag oxides). Indeed, the alumina support stabilizes these highly valent species, but upon reaction, they are short-lived.[20] We excluded from our analysis In/ZrO_2 or other supports rather than γ-Al_2O_3 (SASOL, SCCa-5/200) and RuO_x/Al_2O_3 since it progresses mainly via a DRP side reaction.

When comparing the T_{Tamman} for the active metal or metal oxides used in our catalytic screening and their $X_{CO2} X_{propane}$⁻¹ conversion ratio measured at maximum STY$_{propylene}$ (Figure 6S), we can observe a linear trend. This trend correlates the ability of the material to activate more CO_2 (compared to propane) with catalysts that have a higher oxygen mobility at the reaction conditions (T_{Tamman} < 900 K) and vice versa (Figure 11 top).

The Pearson product moment (correlation strength) linearly correlates T_{Tamman} and $X_{CO2} X_{propane}$⁻¹ with an R = −0.72 (R^2 = 52%) over the full set of data (19 catalysts, hollow and full symbols), and the p-value below 0.001 indicates that the two data significantly correlate with each other. We assume that Au, Ag, and Pt are in the metallic form, while InO_x reduces to the metallic form under reaction conditions (vide infra). Several factors explain the remaining variance in the data: (i) catalytic properties and the mechanism differ; (ii) DRP overestimating the CO_2 consumption; (iii) experimental error at low X; or (iv) particle size (crystallite), which is known to reduce the melting point when small;[76] and (v) erroneous attribution of the crystalline phase, oxidation state, and therefore the T_{Tamman} during the reaction (operando). In fact, Tamman data is estimated on bulk materials under an inert atmosphere, while the supported oxides here—under reaction conditions (H_2 and H_2O in particular)—could significantly alter the mobility.[77,78]

The regression improves further when we exclude the hollow symbols, reaching an R^2 of 74% and p < 0.001, with 16 data points (full symbols). Indeed, Au, Ag, and Pt are unable to form oxides or oxygen vacancies under reaction conditions, therefore imposing an indirect mechanism. In_2O_3, on the contrary, is a stable metal oxide, with T_{Tamman} = 1093 K > $T_{reaction}$, but SEM pictures show redistribution of the external active phase post ODHP and rWGS reactions. Due to the
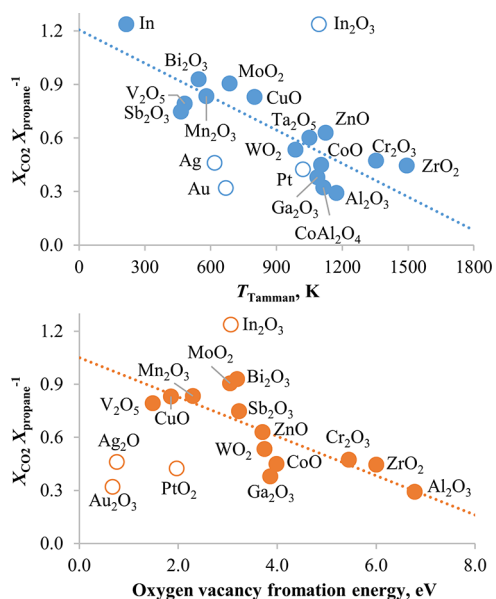
Figure 11. $X_{CO2} X_{propane}^{-1}$ conversion ratios as a function of (top) the Tamman temperature assuming the most stable metal or metal oxides supported on alumina under reaction conditions and (bottom) the oxygen vacancy formation energy for the most stable metal oxides. Conversions at maximum STY of propylene are measured during the T ramp at 0.9 barg (Figure 6S). Hollow symbols: excluded catalysts from regression (In_2O_3; Pt, Au, Ag, and their oxides).

redox environment of the ODHP reaction (H_2 is present in small quantities due to WGS and parallel DHP reactions, while propane abstracts one lattice oxygen, eliminating water and reducing the metal center), we hypothesize that In_2O_3 forms a metallic layer at the interface ($In^{(m)}$: T_{Tamman} = 215 K). This layer is mobile and readily reoxidizable by CO_2, and we think the catalysts undergo in situ equilibrium between the metallic and the oxide form. To support our hypothesis, we decided to study the reducibility properties of selected materials more in detail via H_2 temperature-programmed reduction (H_2-TPR, Figure 12).

All metal oxides show prominent redox properties with H_2 consumption comparable to the loss of 1 molar equiv of oxygen atoms compared to the loading of active metal present (110−118 μmol), except for Galinstan oxides. In this case, reduction was limited to around 28% of the oxygen present (51 μmol of H_2 for a nominal loading of 180 μmol of lattice O of

the active phase). From the literature, H_2 is capable of reducing Ga_2O_3/Al_2O_3, with a distinctive peak centered at 600 °C,[79] and Ga is the major constituent in the Galinstan oxide alloy (78%). Instead, GalinstanO$_x$ presents a broad uptake, without the characteristic peak from pure Ga, further validating its alloy nature and not segregated form. Moreover, volatilization of the reduced metal alloy occurred before the material could reach complete reduction, as we could see a metallic mirror deposit, covering the cold spot in the internal wall of the quartz tube, which biases the results.

Despite this, GalinstanO$_x$ resisted volatilization during our catalytic screening (Figure 7) and converted twice more CO_2 per propane compared to pure GaO$_x$ ($X_{CO2} X_{propane}^{-1}$ = 0.73 vs 0.38), but the overall activity was halved (STY$_{propylene}$ = 4.7 vs 9.6 mol h^{-1} kg$_{cat}^{-1}$). This result further supports our Tamman theory: we tuned the *m.p.* of an active metal (Ga) by alloying with dopants (In, Sn) to lower its T_{Tamman} under redox reaction conditions and shift the mechanism from an indirect catalyst to a direct one. The resulting GalinstanO$_x$ catalyst (T_{Tamman} = 1070 K) partially reduces during ODHP (T_{Tamman} of metallic Galinstan is 127 K) and activates twice more CO_2 per propane than pure GaO$_x$, more than a weighted linear contribution from hypothetically segregated GaO$_x$ and InO$_x$ catalysts ($X_{CO2} X_{propane}^{-1}$ = 0.5).

InO$_x$ shows also a broad uptake of H_2 starting from 200 °C, indicating the absence of ordered crystalline structures, which might explain its peculiar high CO_2 activation during ODHP. InO$_x$ peaks at 600 °C, consuming 60% of the lattice oxygen present (In_2O_3 to $InO_{0.6}$ and $H_2O_{(g)}$). As an important note for future investigations, catalysts with a low *m.p.* might not be applicable if the active material volatilizes, coalesces, and sinters or irreversibly deactivates via Ostwald ripening during longer TOS. However, an appropriate support mitigates this phenomenon, if the metal−support interaction overcomes the spontaneous tendency of low *m.p.* materials to coalesce.[76] In this regard, H_2-TPR volatilized GalinstanO$_x$/Al$_2O_3$ but not InO$_x$/Al$_2O_3$.

CrO$_x$ and VO$_x$ both show distinctive single peaks below 600 °C, indicating the partial reduction of highly valent species to a single crystalline phase. Assuming an initial equimolar mixture of CrO_2 and CrO_3 (brown-copper-red powder) and V_2O_5 (orange-yellow powder) as the main phase of each fresh catalyst, H_2-TPR reduces the materials to Cr_2O_3 (green powder) and $VO_{1.8}$ (black powder), with O stoichiometric coefficients calculated from the H_2 uptake (40% and 30%).
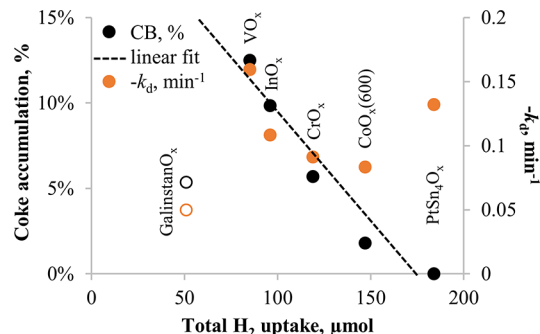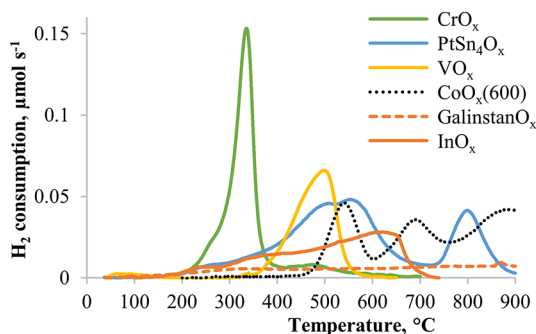

Figure 12. H_2-TPR curves after baseline subtraction (left) and the correlation plot between the curve area and coke accumulation (carbon balance) and the deactivation rate after isothermal reactions at 0.9 barg (RIGHT). We load 100 mg of dry catalyst and flow 10 N mL min^{-1} of 5% H_2 in N_2 at 5 °C min^{-1} from r.t. to 900 °C. A calibrated MS measures and normalizes responses with N_2 as the internal standard. Galinstan oxide (hollow symbols) is not included in the correlation as the material volatilizes and shows incomplete reduction at 900 °C.

Reduction was more severe in the $CoO_x(600)$ catalyst, depleting 95% of the lattice oxygen present in the Co_3O_4 crystalline phase and in $PtSn_4O_x$ it was 107% (assuming the Pt-Sn_4O_8 phase). This indicates that SnO_2 underwent complete reduction, leaving extra H_2 to chemisorb on metallic Pt. Both materials show three main distinctive peaks each, which correlate to the progressive formation of reduced metal oxides and metals.

We tried to correlate the reactivity of indirect (CrO_x and CoO_x) or direct (VO_x and InO_x) mechanism catalysts with H_2-TPR measurements (area, peak T), but unsuccessfully. Contrarily, lower coke accumulation (CB and from CHN analysis of the spent materials) correlated linearly with higher H_2 uptake (R^2 = 94%, Figure 12 right). When comparing different active metal oxides, it is unclear how reducibility can play a role in coke formation, although H_2-TPR is a technique that does not easily differentiate between H_2 that is consumed by a reaction or by adsorption.[80,81] In this regard, it has been shown that the high partial pressure of H_2 induces chemisorption, which prevents hard coke from forming on the surface of the catalyst and favors propylene desorption.[27] That is arguably why the Pt-Sn_4 catalyst (high H_2 uptake) is the material of choice in industrial DHP plants that rely on external heating and aims to minimize coke formation,[82,83] although in our experiments this did not translate to lower deactivation rates. The deactivation rate (k_d) measured during the isothermal tests at 0.9 barg also follows the same trend, with CoO_x (calcined at 600 °C) deviating arguably due to different equilibrations of the active phases at 600 °C (between CoO and Co_2O_3) depending on the redox environment (air calcination, reaction, H_2 atmosphere).

The role of oxygen vacancies in CO_2 reduction over metal oxide-containing catalysts has been widely argued. For example, metal oxides with high oxygen vacancy formation energies have low rWGS activity, while oxygen defect sites on these materials would be highly reactive and lead to fast CO_2 activation. For the (O)DHP reaction, the complete redox catalytic cycle is likely to be limited by the regeneration of such oxygen vacancies, with activities that should correlate with the vacancy formation energy. In this context, we decided to strengthen our empirical Tamman correlation with density functional theory (DFT-PBE/+U, Table 7S). We calculated the lowest vacancy formation energy in bulk metal oxides and correlated it to our experimental results in terms of the ratio of converted CO_2 to propane (Figure 11 bottom).

Lower vacancy formation energies of the bulk metal oxide should compare well with the vacancy formation energy at the *surface* as well because T_{Tamman} < 900 K (enabling oxygen mobility under reaction conditions, Figure 11 top). Similar to the Tamman plot, materials with low oxygen vacancy formation energy correlate with higher ratios of CO_2 converted compared to propane. Regressing the full set of data (hollow and full symbols) leads to no correlation (R^2 = 7%, p = 0.32) because Pt, Au, Ag, and In are not present in the oxide state (hollow symbols). Excluding those catalysts and despite the obvious differences between the crystal structure of active metal oxides and different stoichiometric bulk oxides, we observe a reasonable correlation between the extent of CO_2 reduction/activation and the oxygen vacancy formation energy (full symbols, R^2 = 64%, p < 0.001). Overall, oxygen vacancy alone cannot explain completely the variance in the data of different active metal oxides and reaction mechanisms. The Tamman correlation instead seems to be a better descriptor for this complex system as it is able to account for more key phenomena in this catalytic system.

In this context of oxygen mobility, we hypothesize that for an efficient use of a direct (redox) mechanism (Figure 1, left), catalytic materials need to have apparent reaction rates of ODHP and reoxidation of the same order of magnitude ($r_{ODHP} \approx r_{reoxidation}$). However, one of the drawbacks of CO_2-ODHP vs O_2-ODHP is the imbalance between dehydrogenation and reoxidation kinetic parameters ($E_a^{CO2} > E_a^{propane}$) (Figure 9 top) while requiring the same active sites (pre-exponential factor in Arrhenius-type kinetics, Figure 8S top). For this reason, we need to engineer an active material with a greater number of active sites available for CO_2 reoxidation compared to propane dehydrogenation to balance the two half-cycle kinetics. We think that we can achieve this condition for metal oxides when they operate at reaction $T > T_{Tamman}$ because of bulk atom mobility. If dissociative chemisorption of $CO_{2(g)}$ competes with propane for the same active site, then it would seem we can increase the reactivity with a catalytic material capable of replenishing oxygen vacancies using bulk and neighbor lattice oxygen. The migrated vacancy can then be reoxidized by $CO_{2(g)}$ in a different site. In this context, the spontaneous migration of bulk oxygen species (on a gradient) achieves three improvements. (i) Lattice oxygen can migrate from the bulk of the active material, fill vacancies, and reoxidize the reduced metal center without the need for direct CO_2 reoxidation on the same site, similar to oxygen storage materials in chemical looping processes.[84] (ii) Vacant site diffusion via oxygen mobility constantly exposes fresh sites for $CO_{2(g)}$ reoxidation in sites that are distinct from those for propane dehydrogenation, increasing the chance of CO_2 reaction on a larger surface. As a result, reoxidation with CO_2 proceeds under the steady state since a greater number of active sites (compared to ODHP) compensates for the higher activation energy, balancing the overall kinetics of the direct mechanism. (iii) Additionally, if the elimination of a water molecule occurs before propylene's desorption during the ODHP half-catalytic cycle, we can hypothesize that the newly formed oxygen vacancy now imposes a more electrophilic electronic environment, from which it is more difficult to desorb propylene. However, under oxygen mobility, a neighbor lattice oxygen can occupy the vacancy, increasing the local nucleophilicity and promoting the desorption of propylene.

■ CONCLUSIONS

Our study intended to investigate and reshape the role of CO_2 in oxidative propane dehydrogenation. First, our LCA demonstrates the beneficial environmental impact effects of adding captured CO_2 and highlights the optimal reaction conditions. Based on the current worldwide on-demand propylene production of 26 Mt y^{-1}, revamping the present DHP chemical plants to consume CO_2 via indirect or direct ODHP catalysis could reduce GHG emissions by 8 to 13 Mt_{CO2-eq} y^{-1}. Furthermore, since indirect mechanism catalysts coproduce H_2 and CO, while direct mechanism catalysts coproduce CO, it would avoid synthesizing those gases from steam reforming, achieving negative GHG and FD emissions, at the net, reducing the EI by −70 to −90 Mt_{CO2-eq} y^{-1} and −10 to −20 Mt_{oil-eq} y^{-1}, respectively. In this regard, high selectivity for the coproduct CO (vs H_2) would be the top choice from an EI point of view, which requires a direct mechanism catalyst. The introduction of CO_2 to the gas stream would require a revamping investment to separate and recycle

CO_2 and valorize CO, shifting the OPEX of the process from acquiring a cheap supply of feed material (propane) to an inexpensive energy source (due to the higher endothermic requirements of the ODHP reaction). Additionally, a H_2 generator (water electrolysis) would be required to adjust the H_2/CO ratio necessary for on-site syngas applications, highlighting furthermore the dichotomy between upgrading CO_2 and finding inexpensive and renewable energy sources. In this regard, DRP becomes an added-value side reaction and catalysts that form coke can be integrated into plants that already use in situ regeneration as the heat supply.

These scenarios assume thermodynamic yields and ideal selectivities, thus rendering catalyst design essential. A broad screening of metal oxides, mostly supported on alumina, was performed, focusing on the role and conversion of CO_2, with a close look at reaction selectivities as well as propylene, H_2, and CO space time yields. The screening attempted to classify the catalysts according to their direct or indirect ODHP behavior, and five catalysts were selected for in-depth study, i.e., V, Cr, Co, Ga, and Galinstan oxides. While the chromium oxide catalyst was found to be the most active, it unfortunately rapidly deactivates and follows a clear indirect mechanism. GaO_x followed the same catalytic pathway, but with a lower activity. CoO_x inhibits cracking reactions when doped with K and is selective for DHP and DRP, with minimal coking accumulation, with a clear indirect mechanism dominating. CoO_x does activate at higher T, thus with a lowered activity compared to CrO_x. $PtSn_4O_x$ activated at lower T instead, and it was extremely selective for DHP but converted few CO_2. On the other hand, V, In, Galinstan, Bi, Mo, and Mn oxides do seem to proceed via a direct mechanism, but coking hampers selectivity. BiO_x was stable over time, making it an interesting promoter for the activation of CO_2 via the reverse Boudouard reaction at high temperatures. VO_x and InO_x are the most interesting systems in the presence of CO_2 given their activity and direct mechanism action. InO_x/Al_2O_3 was also found to be an excellent high-temperature rWGS catalyst, which was selective, stable over time, and had a low E_a of 90 kJ mol^{-1} and high activity, reaching equilibrium at 600 °C at GHSV = 30000 mL g$_{cat}$$^{-1}$ h^{-1} with a H_2/CO_2 ratio of 1:1. RWGS conditions reduced InO_x NPs to metallic In and dispersed them into the porosity of the support, while ODHP conditions dispersed the active phase on the external surface.

In this regard, calculating the energy required to form oxygen vacancies alone cannot explain completely the variance in the data of different active metals/metal oxides. Instead, by assessing the Tamman temperature of the active oxide, we discovered that this parameter correlated decently with the ratio of conversion of CO_2 over propane across our broad screening. This better describes this complex system, as it is able to account for more key phenomena, primarily the ability of the active sites to migrate across the support. It seems that a lower Tamman temperature (or thus half the melting temperature of the bulk phase) is a predictor for DHP catalysts to operate more via a direct type of mechanism (D-ODHP) versus an indirect one. With Galinstan for example, we create an alloy that in the metallic form has a lower T_{Tamman} (Δ49 K) compared to Ga. Under reactive ODHP conditions, partial reduction of this mixed oxide likely occurs, which enables bulk atom mobility, and we measure a shift in the mechanism from indirect to direct. In fact, one of the issues of CO_2-ODHP is the imbalance between dehydrogenation and reoxidation rates while requiring the same active sites.

Reoxidation has higher activation energies and requires higher activation temperatures compared to propane dehydrogenation ($E_a^{CO2} > E_a^{propane}$); therefore, we need to engineer an active material with a greater number of active sites available for CO_2 reoxidation to balance the direct mechanism kinetic. We show that metal oxides that operate at reaction $T > T_{Tamman}$ are capable of replenishing oxygen vacancies using bulk lattice oxygen and exhibit a higher CO_2 uptake. Because of the vacancy migration, reoxidation occurs on additional sites on a larger surface, which could balance the overall kinetics of ODHP. Alternatively, with a limited or fixed number of sites, or, e.g., an isolated active cluster, one could focus on better balancing its intrinsic dehydrogenation and reoxidation rates.

In conclusion, we have presented the broadest screening ever for CO_2-assisted (O)DPH over supported oxides and alloys (and a few metals), with a detailed focus on the fate of CO_2 and the selectivity among propylene, H_2, and CO. This allowed a fair comparison across the elements and led to a proposed classification of their reaction along direct or indirect mechanism behavior. Furthermore, when comparing the T_{Tamman} for the active metal/metal oxides used in our catalytic screening and their X_{CO2} $X_{propane}$$^{-1}$ conversion ratio, we observed a statistically significant linear trend, correlating well the ability of a catalyst to activate more CO_2 (compared to propane) with its higher oxygen mobility. This trend can now guide the search for more active and direct mechanism catalysts. Some avenues for future research include mixed-metal catalysts and oxide alloys, allowing T_{Tamman} tuning, but also dopants such as alkali metals to mitigate cracking side reactions and improve the desorption characteristics of propylene. Structured supports like zeolites can potentially isolate low-T_{Tamman} active metal oxides in small pore cages to avoid long-term sintering, volatilization, and stability issues. Moreover, small pore supports may impede hard coke formation of graphitic/polycyclic aromatic compounds by size exclusion, allowing CO_2 to react with soft coke, which is easier to dry reform at lower temperatures. Finally, the role of reducible supports (like CeO_2) or chemical looping materials (CaO, MgO, or transition-metal oxides) could provide additional oxygen vacancy sites for CO_2 activation and possibly oxygen migration to increase the reoxidation rate of direct mechanism catalysts.

■ ASSOCIATED CONTENT

ⓈSupporting Information

The Supporting Information is available free of charge at

Material, methods, and detailed analysis for each active metal tested as well as complementary figures and tables (numbered nS) (PDF)

■ AUTHOR INFORMATION

Corresponding Author

Michiel Dusselier — *Center for Sustainable Catalysis and Engineering (CSCE), KU Leuven, 3001 Heverlee, Belgium;* ⓘ orcid.org/0000-0002-3074-2318;
Email: michiel.dusselier@kuleuven.be

Authors

Marco G. Rigamonti — *Center for Sustainable Catalysis and Engineering (CSCE), KU Leuven, 3001 Heverlee, Belgium;* ⓘ orcid.org/0000-0003-2570-797X

Meera Shah − *Center for Sustainable Catalysis and Engineering (CSCE), KU Leuven, 3001 Heverlee, Belgium*

Thobani G. Gambu − *Laboratory for Chemical Technology, Ghent University, B-9052 Ghent, Belgium*

Mark Saeys − *Laboratory for Chemical Technology, Ghent University, B-9052 Ghent, Belgium;* ⬤ orcid.org/0000-0002-3426-6662

Complete contact information is available at:

■ ACKNOWLEDGMENTS

■ REFERENCES

(1) Agarwal, A.; Sengupta, D.; El-Halwagi, M. Sustainable Process Design Approach for On-Purpose Propylene Production and Intensification. *ACS Sustainable Chem. Eng.* **2018**, *6*, 2407−2421.

(2) Akah, A.; Williams, J.; Ghrami, M. An Overview of Light Olefins Production via Steam Enhanced Catalytic Cracking. *Catal. Surv. Asia* **2019**, *23*, 265−276.

(3) GlobalData. Propylene Industry Installed Capacity and Capital Expenditure (CapEx) Forecast by Region and Countries Including Details of All Active Plants, Planned and Announced Projects, 2025-2021, 2021. https://store.globaldata.com/report/propylene-market-analysis/ (accessed 2022-04-25).

(4) Jiang, X.; Sharma, L.; Fung, V.; Park, S. J.; Jones, C. W.; Sumpter, B. G.; Baltrusaitis, J.; Wu, Z. Oxidative Dehydrogenation of Propane to Propylene with Soft Oxidants via Heterogeneous Catalysis. *ACS Catal.* **2021**, *11*, 2182−2234.

(5) Yang, M.; You, F. Comparative Techno-Economic and Environmental Analysis of Ethylene and Propylene Manufacturing from Wet Shale Gas and Naphtha. *Ind. Eng. Chem. Res.* **2017**, *56*, 4038−4051.

(6) Sternberg, A.; Jens, C. M.; Bardow, A. Life Cycle Assessment of CO2-Based C1-Chemicals. *Green Chem.* **2017**, *19*, 2244−2259.

(7) Zhao, Z.; Liu, Y.; Wang, F.; Li, X.; Deng, S.; Xu, J.; Wei, W.; Wang, F. Life Cycle Assessment of Primary Energy Demand and Greenhouse Gas (GHG) Emissions of Four Propylene Production Pathways in China. *J. Cleaner Prod.* **2017**, *163*, 285−292.

(8) Hawkes, A.; Balcombe, P.; Giarola, S.; Budinis, S. International Energy Agency, Greenhouse Gas R&D Programme. Sustainability in petrochemicals. IEAGHG Technical Report, 2019. http://documents.ieaghg.org/index.php/s/EzPEprswOvaXcx (accessed 2022-04-25).

(9) Lv, L.; Song, G.; Zhao, X.; Chen, J. Environmental Burdens of China's Propylene Manufacturing: Comparative Life-Cycle Assessment and Scenario Analysis. *Sci. Total Environ.* **2021**, *799*, No. 149451.

(10) Rodríguez-Vallejo, D. F.; Guillén-Gosálbez, G.; Chachuat, B. What Is the True Cost of Producing Propylene from Methanol? The Role of Externalities. *ACS Sustainable Chem. Eng.* **2020**, *8*, 3072−3081.

(11) Dubois, J.-L.; Patience, G. S.; Millet, J.-M. M. Propane-Selective Oxidation to Acrylic Acid. *Nanotechnol. Catal.* **2017**, 503−536.

(12) Maddah, H. A. A Comparative Study between Propane Dehydrogenation (PDH) Technologies and Plants in Saudi Arabia. *Am. Acad. Sci. Res. J. Eng. Technol. Sci.* **2018**, *45*, 49−63.

(13) Nawaz, Z. Light Alkane Dehydrogenation to Light Olefin Technologies: A Comprehensive Review. *Rev. Chem. Eng.* **2015**, *31*, 413−436.

(14) Sanfilippo, D.; Miracca, I.; Trifirò, F. Processi Di Deidrogenazione. In *Enciclopedia Degli Idrocarburi* Treccani, 2006; pp 687−699.

(15) Shtyka, O.; Maniukiewicz, W.; Ciesielski, R.; Kedziora, A.; Shatsila, V.; Sierański, T.; Maniecki, T. The Formation of Cr-Al Spinel under a Reductive Atmosphere. *Materials* **2021**, *14*, 3218.

(16) Puurunen, R. L.; Weckhuysen, B. M. Spectroscopic Study on the Irreversible Deactivation of Chromia/Alumina Dehydrogenation Catalysts. *J. Catal.* **2002**, *210*, 418−430.

(17) Iglesias-Juez, A.; Beale, A. M.; Maaijen, K.; Weng, T. C.; Glatzel, P.; Weckhuysen, B. M. A Combined in Situ Time-Resolved UV-Vis, Raman and High-Energy Resolution X-Ray Absorption Spectroscopy Study on the Deactivation Behavior of Pt and PtSn Propane Dehydrogenation Catalysts under Industrial Reaction Conditions. *J. Catal.* **2010**, *276*, 268−279.

(18) Im, J.; Choi, M. Physicochemical Stabilization of Pt against Sintering for a Dehydrogenation Catalyst with High Activity, Selectivity, and Durability. *ACS Catal.* **2016**, *6*, 2819−2826.

(19) Węgrzyniak, A.; Jarczewski, S.; Węgrzynowicz, A.; Michorczyk, B.; Kuśtrowski, P.; Michorczyk, P. Catalytic Behavior of Chromium Oxide Supported on Nanocasting-Prepared Mesoporous Alumina in Dehydrogenation of Propane. *Nanomaterials* **2017**, *7*, 249.

(20) Cavani, F.; Koutyrev, M.; Trifirò, F.; Bartolini, A.; Ghisletti, D.; Iezzi, R.; Santucci, A.; Del Piero, G. Chemical and Physical Characterization of Alumina-Supported Chromia-Based Catalysts and Their Activity in Dehydrogenation of Isobutane. *J. Catal.* **1996**, *158*, 236−250.

(21) Gascón, J.; Téllez, C.; Herguido, J.; Menéndez, M. Propane Dehydrogenation over a Cr2O3/Al2O3 Catalyst: Transient Kinetic Modeling of Propene and Coke Formation. *Appl. Catal., A* **2003**, *248*, 105−116.

(22) Huš, M.; Kopač, D.; Likozar, B. Kinetics of Non-Oxidative Propane Dehydrogenation on Cr2O3 and the Nature of Catalyst Deactivation from First-Principles Simulations. *J. Catal.* **2020**, *386*, 126−138.

(23) Weckhuysen, B. M.; Bensalem, A.; Schoonheydt, R. A. In Situ UV−VIS Diffuse Reflectance Spectroscopy-on-Line Activity Measurements: Significance of Crn+ Species (n = 2, 3 and 6) in n-Butane Dehydrogenation Catalyzed by Supported Chromium Oxide Catalysts. *J. Chem. Soc., Faraday Trans.* **1998**, *94*, 2011−2014.

(24) Agafonov, Y. A.; Gaidai, N. A.; Lapidus, A. L. Influence of the Preparation Conditions for Catalysts CrO x /SiO2 on Their Efficiency in Propane Dehydrogenation in the Presence CO2. *Russ. Chem. Bull.* **2014**, *63*, 381−388.

(25) Michorczyk, P.; Ogonowski, J.; Zeńczak, K. Activity of Chromium Oxide Deposited on Different Silica Supports in the Dehydrogenation of Propane with CO2 - A Comparative Study. *J. Mol. Catal. A: Chem.* **2011**, *349*, 1−12.

(26) Michorczyk, P.; Ogonowski, J.; Niemczyk, M. Investigation of Catalytic Activity of CrSBA-1 Materials Obtained by Direct Method in the Dehydrogenation of Propane with CO2. *Appl. Catal., A* **2010**, *374*, 142−149.

(27) Li, Q.; Sui, Z.; Zhou, X.; Zhu, Y.; Zhou, J.; Chen, D. Coke Formation on Pt-Sn/Al2O3 Catalyst in Propane Dehydrogenation: Coke Characterization and Kinetic Study. *Top. Catal.* **2011**, *54*, 888−896.

(28) Lapidus, A. L.; Agafonov, Y. A.; Gaidai, N. A.; Trushin, D. V.; Nekrasov, N. V. Effect of the Introduction of Alkaline Promoters into

Chromium Oxide Catalysts for Propane Dehydrogenation in the Presence of CO 2. *Solid Fuel Chem.* **2012**, *46*, 14−22.

(29) Resasco, D. E.; Haller, G. L. Catalytic Dehydrogenation of Lower Alkanes. *Catalysis* **2007**, 379−411.

(30) Atanga, M. A.; Rezaei, F.; Jawad, A.; Fitch, M.; Rownaghi, A. A. Oxidative Dehydrogenation of Propane to Propylene with Carbon Dioxide. *Appl. Catal., B* **2018**, *220*, 429−445.

(31) Pirro, L.; Obradović, A.; Vandegehuchte, B. D.; Marin, G. B.; Thybaut, J. W. Model-Based Catalyst Selection for the Oxidative Coupling of Methane in an Adiabatic Fixed-Bed Reactor. *Ind. Eng. Chem. Res.* **2018**, *57*, 16295−16307.

(32) Michorczyk, P.; Zeńczak, K.; Niekurzak, R.; Ogonowski, J. Dehydrogenation of Propane with CO2 - A New Green Process for Propene and Synthesis Gas Production. *Pol. J. Chem. Technol.* **2012**, *14*, 77−82.

(33) Ansari, M. B.; Park, S.-E. Carbon Dioxide Utilization as a Soft Oxidant and Promoter in Catalysis. *Energy Environ. Sci.* **2012**, *5*, 9419.

(34) Grant, J. T.; Carrero, C. A.; Goeltl, F.; Venegas, J.; Mueller, P.; Burt, S. P.; Specht, S. E.; McDermott, W. P.; Chieregato, A.; Hermans, I. Selective Oxidative Dehydrogenation of Propane to Propene Using Boron Nitride Catalysts. *Science* **2016**, *354*, 1570−1573.

(35) Venegas, J. M.; Zhang, Z.; Agbi, T. O.; McDermott, W. P.; Alexandrova, A.; Hermans, I. Why Boron Nitride Is Such a Selective Catalyst for the Oxidative Dehydrogenation of Propane. *Angew. Chem., Int. Ed.* **2020**, *59*, 16527−16535.

(36) Raju, G.; Reddy, B. M.; Park, S. E. CO2 Promoted Oxidative Dehydrogenation of N-Butane over VO x/MO2-ZrO2 (M = Ce or Ti) Catalysts. *J. CO2 Util.* **2014**, *5*, 41−46.

(37) Chen, K.; Bell, A. T.; Iglesia, E. Kinetics and Mechanism of Oxidative Dehydrogenation of Propane on Vanadium, Molybdenum, and Tungsten Oxides. *J. Phys. Chem. B* **2000**, *104*, 1292−1299.

(38) Rostom, S.; de Lasa, H. Propane Oxidative Dehydrogenation on Vanadium-Based Catalysts under Oxygen-Free Atmospheres. *Catalysts* **2020**, *10*, 418.

(39) Chen, K. D.; Khodakov, A.; Yang, J.; Bell, A.; Iglesia, E. Isotopic Tracer Studies of Oxidative Dehydrogenation Pathways on Mo-Based Catalysts. *J. Catal.* **1999**, *186*, 325−333.

(40) Liu, H.; Zhang, Z.; Li, H.; Huang, Q. Intrinsic Kinetics of Oxidative Dehydrogenation of Propane in the Presence of CO2 over Cr/MSU-1 Catalyst. *J. Nat. Gas Chem.* **2011**, *20*, 311−317.

(41) Takehira, K.; Ohishi, Y.; Shishido, T.; Kawabata, T.; Takaki, K.; Zhang, Q.; Wang, Y. Behavior of Active Sites on Cr-MCM-41 Catalysts during the Dehydrogenation of Propane with CO2. *J. Catal.* **2004**, *224*, 404−416.

(42) Michorczyk, P.; Pietrzyk, P.; Ogonowski, J. Preparation and Characterization of SBA-1-Supported Chromium Oxide Catalysts for CO 2 Assisted Dehydrogenation of Propane. *Microporous Mesoporous Mater.* **2012**, *161*, 56−66.

(43) XU, B.; ZHENG, B.; HUA, W.; YUE, Y.; GAO, Z. Support Effect in Dehydrogenation of Propane in the Presence of CO2 over Supported Gallium Oxide Catalysts. *J. Catal.* **2006**, *239*, 470−477.

(44) Chen, M.; Xu, J.; Cao, Y.; He, H.-Y.; Fan, K.-N.; Zhuang, J.-H. Dehydrogenation of Propane over In2O3−Al2O3 Mixed Oxide in the Presence of Carbon Dioxide. *J. Catal.* **2010**, *272*, 101−108.

(45) Michorczyk, P.; Kuśtrowski, P.; Chmielarz, L.; Ogonowski, J. Influence of Redox Properties on the Activity of Iron Oxide Catalysts in Dehydrogenation of Propane with CO2. *React. Kinet. Catal. Lett.* **2004**, *82*, 121−130.

(46) Ren, Y.; Wang, J.; Hua, W.; Yue, Y.; Gao, Z. Ga 2O 3/HZSM-48 for Dehydrogenation of Propane: Effect of Acidity and Pore Geometry of Support. *J. Ind. Eng. Chem.* **2012**, *18*, 731−736.

(47) Agafonov, Y. A.; Gaidai, N. A.; Lapidus, A. L. Propane Dehydrogenation on Chromium Oxide and Gallium Oxide Catalysts in the Presence of CO2. *Kinet. Catal.* **2018**, *59*, 744−753.

(48) Shishido, T.; Shimamura, K.; Teramura, K.; Tanaka, T. Role of CO2 in Dehydrogenation of Propane over Cr-Based Catalysts. *Catal. Today* **2012**, *185*, 151−156.

(49) Dong, S.; Altvater, N. R.; Mark, L. O.; Hermans, I. Assessment and Comparison of Ordered & Non-Ordered Supported Metal Oxide Catalysts for Upgrading Propane to Propylene. *Appl. Catal., A* **2021**, *617*, No. 118121.

(50) Siahvashi, A.; Chesterfield, D.; Adesina, A. A. Propane CO2 (Dry) Reforming over Bimetallic Mo-Ni/Al2O3 Catalyst. *Chem. Eng. Sci.* **2013**, *93*, 313−325.

(51) Boffito, D. C.; Fernandez Rivas, D. Process Intensification Connects Scales and Disciplines towards Sustainability. *Can. J. Chem. Eng.* **2020**, *98*, 2489−2506.

(52) Mauhar, S. M.; Barjaktarović, B. G.; Sovilj, M. N. Optimization of Propylene - Propane Distillation Process. *Chem. Pap.* **2004**, *58*, 386−390.

(53) Grande, C. A.; Rodrigues, A. E. Propane/Propylene Separation by Pressure Swing Adsorption Using Zeolite 4A. *Ind. Eng. Chem. Res.* **2005**, *44*, 8815−8829.

(54) Siqueira, R. M.; Freitas, G. R.; Peixoto, H. R.; Nascimento, J. F.; do Musse, A. P. S.; Torres, A. E. B.; Azevedo, D. C. S.; Bastos-Neto, M. Carbon Dioxide Capture by Pressure Swing Adsorption. *Energy Procedia* **2017**, *114*, 2182−2192.

(55) Aoki, K.; Kusakabe, K.; Morooka, S. Separation of Gases with an A-Type Zeolite Membrane. *Ind. Eng. Chem. Res.* **2000**, *39*, 2245−2251.

(56) Dusselier, M.; Davis, M. E. Small-Pore Zeolites: Synthesis and Catalysis. *Chem. Rev.* **2018**, *118*, 5265−5329.

(57) Munnik, P.; De Jongh, P. E.; De Jong, K. P. Recent Developments in the Synthesis of Supported Catalysts. *Chem. Rev.* **2015**, *115*, 6687−6718.

(58) Chen, M.; Xu, J.; Liu, Y.-M. M.; Cao, Y.; He, H.-Y. Y.; Zhuang, J.-H. H. Supported Indium Oxide as Novel Efficient Catalysts for Dehydrogenation of Propane with Carbon Dioxide. *Appl. Catal., A* **2010**, *377*, 35−41.

(59) Chen, K.; Iglesia, E.; Bell, A. T. Kinetic Isotopic Effects in Oxidative Dehydrogenation of Propane on Vanadium Oxide Catalysts. *J. Catal.* **2000**, *192*, 197−203.

(60) Aly, M.; Fornero, E. L.; Leon-Garzon, A. R.; Galvita, V. V.; Saeys, M. Effect of Boron Promotion on Coke Formation during Propane Dehydrogenation over Pt/γ-Al2O3 Catalysts. *ACS Catal.* **2020**, *10*, 5208−5216.

(61) Muhammad, I.; Makwashi, N.; Manos, G. Catalytic Degradation of Linear Low-Density Polyethylene over HY-Zeolite via Pre-Degradation Method. *J. Anal. Appl. Pyrol.* **2019**, *138*, 10−21.

(62) Wolf, M.; Raman, N.; Taccardi, N.; Haumann, M.; Wasserscheid, P. Coke Formation during Propane Dehydrogenation over Ga−Rh Supported Catalytically Active Liquid Metal Solutions. *ChemCatChem* **2020**, *12*, 1085−1094.

(63) Sakurai, Y.; Suzaki, T.; Nakagawa, K.; Ikenaga, N. oki.; Aota, H.; Suzuki, T. Oxidation Capability of Carbon Dioxide in the Dehydrogenation of Ethylbenzene over Vanadium Oxide-Loaded MgO Catalyst. *Chem. Lett.* **2000**, *29*, 526−527.

(64) Bremmer, G. M.; Zacharaki, E.; Sjåstad, A. O.; Navarro, V.; Frenken, J. W. M.; Kooyman, P. J. In Situ TEM Observation of the Boudouard Reaction: Multi-Layered Graphene Formation from CO on Cobalt Nanoparticles at Atmospheric Pressure. *Faraday Discuss.* **2017**, *197*, 337−351.

(65) Carnevali, D.; D'Oliveira, A.; Rigamonti, M. G.; Cavani, F.; Patience, G. S. Pt-WO3 Oxydehydrates Fructose to Furans in the Gas Phase. *Chem. Eng. J.* **2021**, *429*, No. 132337.

(66) Cendejas, M. C.; Dorn, R. W.; McDermott, W. P.; Lebrón-Rodríguez, E. A.; Mark, L. O.; Rossini, A. J.; Hermans, I. Controlled Grafting Synthesis of Silica-Supported Boron for Oxidative Dehydrogenation Catalysis. *J. Phys. Chem. C* **2021**, *125*, 12636−12649.

(67) Daza, Y. A.; Kuhn, J. N. CO2 Conversion by Reverse Water Gas Shift Catalysis: Comparison of Catalysts, Mechanisms and Their Consequences for CO2 Conversion to Liquid Fuels. *RSC Adv.* **2016**, *6*, 49675−49691.

(68) Sun, Q.; Ye, J.; Liu, C.; Ge, Q. In2O3 as a Promising Catalyst for CO2 Utilization: A Case Study with Reverse Water Gas Shift over In2O3. *Greenhouse Gases: Sci. Technol.* **2014**, *4*, 140−144.

(69) Frei, M. S.; Mondelli, C.; García-Muelas, R.; Kley, K. S.; Puértolas, B.; López, N.; Safonova, O. V.; Stewart, J. A.; Curulla Ferré, D.; Pérez-Ramírez, J. Atomic-Scale Engineering of Indium Oxide Promotion by Palladium for Methanol Production via CO2 Hydrogenation. *Nat. Commun.* **2019**, *10*, No. 3377.

(70) Zhu, M.; Wachs, I. E. Iron-Based Catalysts for the High-Temperature Water−Gas Shift (HT-WGS) Reaction: A Review. *ACS Catal.* **2016**, *6*, 722−732.

(71) Pastor-Pérez, L.; Shah, M.; le Saché, E.; Ramirez Reina, T. Improving Fe/Al2O3 Catalysts for the Reverse Water-Gas Shift Reaction: On the Effect of Cs as Activity/Selectivity Promoter. *Catalysts* **2018**, *8*, 608.

(72) Schäferhans, J.; Gõmez-Quero, S.; Andreeva, D. V.; Rothenberg, G. Novel and Effective Copper-Aluminum Propane Dehydrogenation Catalysts. *Chem. − Eur. J.* **2011**, *17*, 12254−12256.

(73) Prašnikar, A.; Pavlišič, A.; Ruiz-Zepeda, F.; Kovač, J.; Likozar, B. Mechanisms of Copper-Based Catalyst Deactivation during CO2 Reduction to Methanol. *Ind. Eng. Chem. Res.* **2019**, *58*, 13021−13029.

(74) Dang, S.; Qin, B.; Yang, Y.; Wang, H.; Cai, J.; Han, Y.; Li, S.; Gao, P.; Sun, Y. Rationally Designed Indium Oxide Catalysts for CO2 Hydrogenation to Methanol with High Activity and Selectivity. *Sci. Adv.* **2020**, *6* (). DOI: 10.1126/sciadv.aaz2060.

(75) Zuo, Z.; Liu, S.; Wang, Z.; Liu, C.; Huang, W.; Huang, J.; Liu, P. Dry Reforming of Methane on Single-Site Ni/MgO Catalysts: Importance of Site Confinement. *ACS Catal.* **2018**, *8*, 9821−9835.

(76) Dai, Y.; Lu, P.; Cao, Z.; Campbell, C. T.; Xia, Y. The Physical Chemistry and Materials Science behind Sinter-Resistant Catalysts. *Chem. Soc. Rev.* **2018**, *47*, 4314−4331.

(77) Wang, C. B.; Cai, Y.; Wachs, I. E. Reaction-Induced Spreading of Metal Oxides onto Surfaces of Oxide Supports during Alcohol Oxidation: Phenomenon, Nature, and Mechanisms. *Langmuir* **1999**, *15*, 1223−1235.

(78) Wachs, I. E.; Jehng, J. M.; Ueda, W. Determination of the Chemical Nature of Active Surface Sites Present on Bulk Mixed Metal Oxide Catalysts. *J. Phys. Chem. B* **2005**, *109*, 2275−2284.

(79) Shao, C.-T.; Lang, W.-Z.; Yan, X.; Guo, Y.-J. Catalytic Performance of Gallium Oxide Based-Catalysts for the Propane Dehydrogenation Reaction: Effects of Support and Loading Amount. *RSC Adv.* **2017**, *7*, 4710−4723.

(80) Seguel, J.; García, R.; Chimentão, R. J.; García-Fierro, J. L.; Ghampson, I. T.; Escalona, N.; Sepúlveda, C. Thermal Modification Effect on Supported Cu-Based Activated Carbon Catalyst in Hydrogenolysis of Glycerol. *Materials* **2020**, *13*, 603.

(81) Kim, K.; Kang, D. W.; Choi, Y.; Kim, W.; Lee, H.; Lee, J. W. Improved H2utilization by Pd Doping in Cobalt Catalysts for Reductive Amination of Polypropylene Glycol. *RSC Adv.* **2020**, *10*, 45159−45169.

(82) Bariås, O. A.; Holmen, A.; Blekkan, E. A. Propane Dehydrogenation over Supported Pt and Pt−Sn Catalysts: Catalyst Preparation, Characterization, and Activity Measurements. *J. Catal.* **1996**, *158*, 1−12.

(83) Zhou, H.; Gong, J.; Xu, B.; Deng, S.; Ding, Y.; Yu, L.; Fan, Y. PtSnNa/SUZ-4: An Efficient Catalyst for Propane Dehydrogenation. *Chin. J. Catal.* **2017**, *38*, 529−536.

(84) Imtiaz, Q.; Kurlov, A.; Rupp, J. L. M.; Müller, C. R. Highly Efficient Oxygen-Storage Material with Intrinsic Coke Resistance for Chemical Looping Combustion-Based CO2 Capture. *ChemSusChem* **2015**, *8*, 2055−2065.